

***c*-axis transport in UTe<sub>2</sub>: Evidence of three-dimensional conductivity component**

Yun Suk Eo<sup>1</sup>,<sup>✉</sup> Shouzheng Liu,<sup>2</sup> Shanta R. Saha,<sup>1</sup> Hyunsoo Kim,<sup>1,\*</sup> Sheng Ran,<sup>1,3,†</sup> Jarryd A. Horn<sup>1</sup>,<sup>✉</sup> Halyna Hodovanets<sup>1,\*</sup>, John Collini,<sup>1</sup> Tristin Metz,<sup>1</sup> Wesley T. Fuhrman,<sup>1</sup> Andriy H. Nevidomskyy,<sup>4</sup> Jonathan D. Denlinger,<sup>5</sup> Nicholas P. Butch,<sup>1,3</sup> Michael S. Fuhrer,<sup>6,7</sup> L. Andrew Wray,<sup>2</sup> and Johnpierre Paglione<sup>1,8,‡</sup>

<sup>1</sup>Maryland Quantum Materials Center and Department of Physics, University of Maryland, College Park, Maryland 20742, USA

<sup>2</sup>Department of Physics, New York University, New York, New York 10003, USA

<sup>3</sup>NIST Center for Neutron Research, National Institute of Standards and Technology, Gaithersburg, Maryland 20899, USA

<sup>4</sup>Department of Physics and Astronomy, Rice University, Houston, Texas 77005, USA

<sup>5</sup>Advanced Light Source, Lawrence Berkeley National Laboratory, Berkeley, California 94720, USA

<sup>6</sup>School of Physics and Astronomy, Monash University, Victoria 3800, Australia

<sup>7</sup>ARC Centre of Excellence in Future Low-Energy Electronics Technologies, Monash University, Victoria 3800, Australia

<sup>8</sup>Canadian Institute for Advanced Research, Toronto, Ontario, Canada M5G 1Z8



(Received 25 January 2021; accepted 1 August 2022; published 24 August 2022)

We study the temperature dependence of electrical resistivity for currents directed along all crystallographic axes of the spin-triplet superconductor UTe<sub>2</sub>. We focus particularly on an accurate determination of the resistivity along the *c* axis ( $\rho_c$ ) by using a generalized Montgomery technique that allows extraction of crystallographic resistivity components from a single sample. In contrast to expectations from the observed highly anisotropic band structure, our measurement of the absolute values of resistivities in all current directions reveals a surprisingly nearly isotropic transport behavior at temperatures above Kondo coherence, with  $\rho_c \sim \rho_b \sim 2\rho_a$ , that evolves to reveal qualitatively distinct behaviors on cooling. The temperature dependence of  $\rho_c$  exhibits a peak at a temperature much lower than the onset of Kondo coherence observed in  $\rho_a$  and  $\rho_b$ , consistent with features in magnetotransport and magnetization that point to a magnetic origin. A comparison to the temperature-dependent evolution of the scattering rate observed in angle-resolved photoemission spectroscopy experiments provides important insights into the underlying electronic structure necessary for building a microscopic model of superconductivity in UTe<sub>2</sub>.

DOI: [10.1103/PhysRevB.106.L060505](https://doi.org/10.1103/PhysRevB.106.L060505)

The recently discovered superconductivity in UTe<sub>2</sub> [1] is believed to be a strong contender for spin-triplet Cooper pairing driven by ferromagnetic spin fluctuations, as suggested by scaling of magnetization data [1], muon spin relaxation experiments [2], and an upper critical field that greatly exceeds the Pauli paramagnetic limit along all principal axes [1]. A point-nodal structure in the superconducting gap is evidenced by studies of thermal conductivity and penetration depth [3], and the temperature dependence of the Knight shift in nuclear magnetic resonance is weak, which is consistent with the degeneracy existing in the spin-triplet state [1,4]. Other fascinating properties including reentrant superconductivity [5,6] and pressure-induced multiple superconducting phases [7,8] signal a rich superconducting state in UTe<sub>2</sub>. Observations of a split transition in thermodynamic critical temperature  $T_c$  at ambient pressure and the existence of the Kerr effect at  $T_c$ , indicating breaking of time-reversal symmetry in the superconducting state, point to a two-component order parameter, expected in a topological Weyl superconductor [9,10].

Together with observations of novel surface states [11,12], magnetic excitation spectra [13–16], and tunability of the transition temperature and splitting [17,18], the plethora of interesting phenomena in UTe<sub>2</sub> will require continued attention to the details of this fascinating system [19].

To date, the majority of experiments have focused on elucidating the symmetry and topological class of the superconducting order parameter, or probing the landscape of proximate ground states, such as magnetism [7,8,21–24]. However, how the Fermi surface forms by the chains of uranium and tellurium atoms along the *a* and *b* axes, respectively, as shown in Fig. 1(a), together with Kondo physics and *f*-electron contributions remains an open question. Band calculations seem to depend sensitively on the on-site Coulomb interaction strength  $U_{\text{int}}$  and the role of *f*-electron physics. Local density approximation (LDA) calculations suggested that the normal state of UTe<sub>2</sub> is a semimetal [25,26], while more recent LDA+*U* calculations find that an insulator-to-metal evolution can be tuned by the strength of  $U_{\text{int}}$ , with two perpendicular Fermi surface (FS) sheets forming a quasi-two-dimensional (quasi-2D) FS emerging when  $U_{\text{int}}$  is tuned to  $\sim 2$  eV [27,28]. Recent angle-resolved photoemission spectroscopy (ARPES) experiments at 20 K indeed observed this 2D FS in addition to a more three-dimensional (3D) *f*-like pocket surrounding the *Z* point (*Z* pocket) [20], as shown schematically in Figs. 1(b) and 1(c). Importantly, and without

\*Present Address: Department of Physics, Missouri University of Science and Technology, Rolla, Missouri 65409, USA.

†Present address: Department of Physics, Washington University in St. Louis, St. Louis, Missouri 63130, USA.

‡paglione@umd.edu

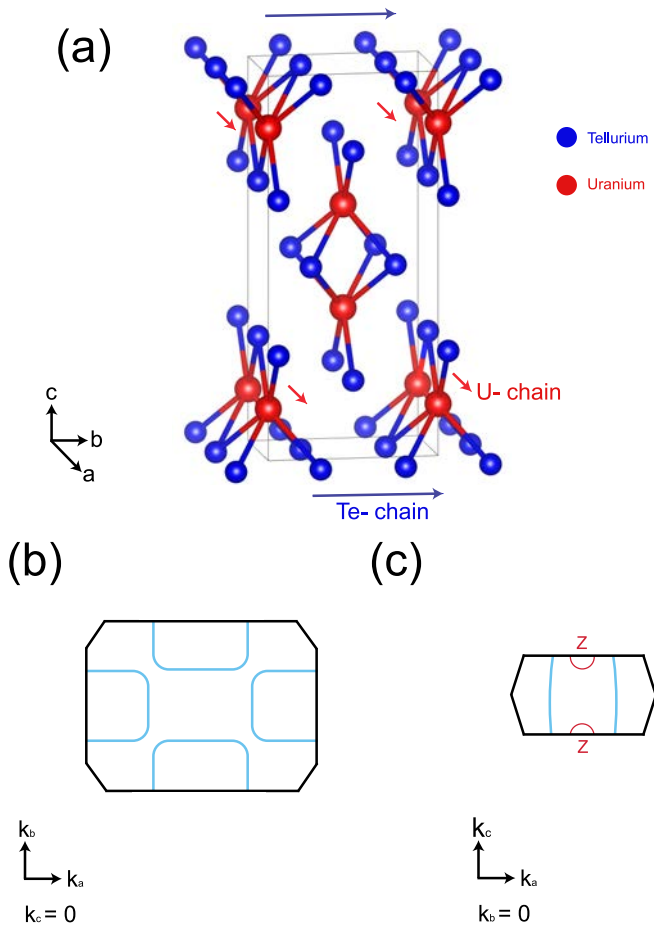


FIG. 1. UTe<sub>2</sub> crystal structure and Fermi surface. (a) Crystal structure of UTe<sub>2</sub>;  $a = 4.161$  Å,  $b = 6.122$  Å,  $c = 13.955$  Å. (b) Schematic picture of the rectangular Fermi pockets (shown in blue) in the  $a$ - $b$  plane of the BZ (based on Ref. [20]). (c) Schematic picture of the Z pocket in the presence of the less dispersive rectangular pocket in the  $a$ - $c$  plane of the BZ (based on Ref. [20]).

the need to invoke  $U_{\text{int}}$ , density functional theory combined with dynamical mean-field theory (DFT + DMFT) band calculations in the same study suggest that the two sets of sheets comprising the quasi-2D FS derive from the U-6*d* and Te-5*p* orbitals of the two perpendicular chains of uranium and tellurium atoms [Fig. 1(a)], but they fail to predict the existence of the  $f$ -like Z pocket, leaving the role of 5*f* electrons unanswered.

Given the confluence of interaction- and dimension-dependent contributions to the normal state electronic behavior in UTe<sub>2</sub>, it is imperative to have an accurate measure and understanding of the conductivity anisotropy in this system in order to understand the Fermiology that leads to pairing. Here, we accurately determine the electrical resistivity along all primary crystallographic directions in UTe<sub>2</sub>, focusing on the so-far elusive  $c$ -axis transport behavior in order to help elucidate the role of dimensionality and orbital contributions to the normal state electronics. We compare the measured transport anisotropy and its temperature dependences with ARPES in order to better connect peculiar behaviors with specific band components, providing a consistent picture of transport in

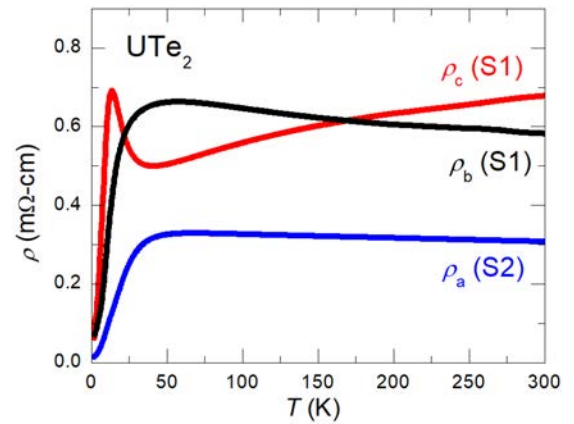


FIG. 2. Electrical resistivity of UTe<sub>2</sub> extracted using a generalized Montgomery measurement technique on two crystalline samples, including a diamond-shaped sample with  $b$ - $c$  plane orientation (sample S1) and a nearly-rectangular-shaped sample with  $a$ - $c$  plane orientation (sample S2). Absolute resistivities are obtained by extracting principal components of resistivities from a combination of resistance measurement geometries and numerical modeling (see SM [29] for more details, including extracted  $\rho_c$  data for sample S2 and sample photos in Fig. S3).

UTe<sub>2</sub>. Furthermore, our magnetotransport analysis suggests magnetism as a potential origin of the qualitatively anisotropic scattering behavior at low temperatures.

Although it is common to study transport anisotropy using the Montgomery technique [30], which allows extraction of two components of the resistivity tensor from a single rectangular-shaped sample, in a highly anisotropic system the possible misalignment between the sample geometry edge and crystal axis can lead to spurious results, mixing low- and high-conductivity channels that introduce large errors when converting to resistivity. We utilize a generalized (i.e., non-rectangular) Montgomery technique, where electrical contacts are placed on corners of a sample with currents directed along a mixture of principal axis directions, and employ finite element analysis to extract the principal components. We present data from a diamond-shaped sample with  $b$ - $c$  plane orientation (sample S1) and a rectangular-shaped sample with  $a$ - $c$  plane orientation (sample S2). (Details of the transport setup and considerations, sample geometries, and detailed analysis are found in Supplemental Material (SM) [29] Secs. I and II.) By comparing the  $c$ -axis components measured in the two samples, we obtain an accurate absolute measurement of the  $c$ -axis resistivity and rule out the possibility of misinterpreting its magnitude, which has been a known issue in other quasi-2D materials [31].

Figure 2 presents the extracted resistivities for all three primary crystal directions, allowing analysis of the quantitative anisotropy. Our results are qualitatively consistent with the previous studies reporting  $\rho_a$  and  $\rho_b$ , but quantitatively different by up to a factor of  $\sim 2$  [1,25]. In contrast to the naive expectations for the quasi-2D Fermi surfaces of UTe<sub>2</sub>, the nearly isotropic conductivities as observed in the highly anisotropic metal in the normal state of Sr<sub>2</sub>RuO<sub>4</sub> [32] can only be explained by the presence of a much more isotropic Fermi

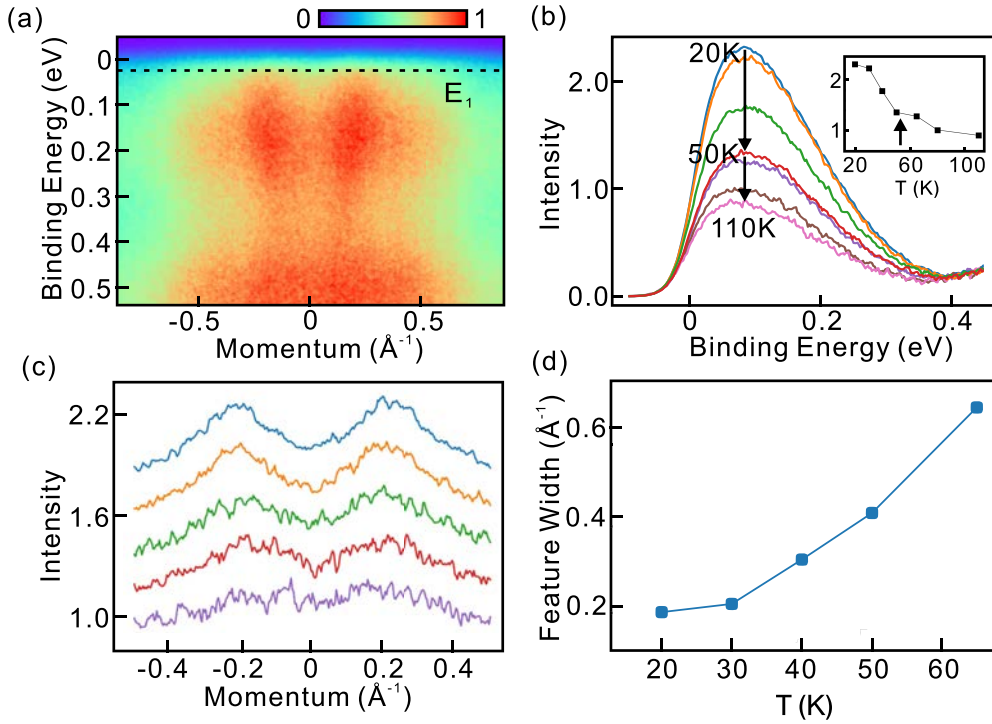


FIG. 3. Temperature dependence of ARPES. (a) An ARPES image of the UTe<sub>2</sub> 6d bands, measured at 20 K along the  $\Gamma$ -X axis at  $h\nu = 74$  eV, in normal emission from the [011] crystal face. (b) Temperature (Temp) dependence of quasielastically scattered photoelectrons. ARPES intensity on the uranium O-edge resonance ( $h\nu = 110$  eV) was integrated in a region with no visible bands [from  $k = 0.6$  Å<sup>-1</sup> to  $k = 1.0$  Å<sup>-1</sup>]. (c) Momentum distribution curves (MDCs) of 6d band electrons at 25 meV, measured at  $h\nu = 74$  eV and temperatures of 20, 30, 40, 50, and 65 K, from top to bottom. (d) The feature width from Lorentzian fits (see SM [29] Sec. VII for details) of the MDCs in (c), used for comparison with resistivity (see text).

surface component. Here, we employ a simple two-channel Drude model as a start, finding quantitative agreement with the available ARPES data [20]. In this model, we assume that the conductivity consists of two conduction channels, one 2D and one 3D, corresponding to the U-6d and Te-5p derived FS sheets and the isotropic highly U- $f$ -weighted Z pocket, respectively, as depicted in Fig. 1. The conductivity along the  $a$  axis is composed of two contributions:

$$\sigma_{ab} = \sigma_{2D} + \sigma_Z. \quad (1)$$

Since the rectangular pockets are weakly dispersive in the  $c$ -axis direction, we ignore their contribution and only consider the Z pocket, i.e.,  $\sigma_c \approx \sigma_Z$ . Using the Drude picture for transport, we can compare the transport data with ARPES data using an equation for the contribution of the 2D-like rectangular pocket along the  $a$ -axis direction,

$$\sigma_{2D} \approx 1/\rho_a - 1/\rho_c = 2n_{2D}e\mu_{2D}, \quad (2)$$

where  $n_{2D}$ ,  $m_{2D}$ , and  $\mu_{2D}$  refer to the carrier density, effective mass, and mobility of the 2D Fermi surfaces, respectively. The factor of 2 originates from the fact that two rectangular pockets exist in the Brillouin zone (BZ). We estimate the ARPES parameters [right side of Eq. (2)] from the uranium 6d band dispersion, which predominantly contributes to the transport along the (U chain)  $a$  axis (see SM [29] Sec. VI for details). By comparing these two experiments, we estimate a mean free path  $l_{2D} \approx 19$  Å at 20 K, or a mobility of  $1.8$  cm<sup>2</sup>/(V s). Using the momentum distribution curves (MDCs) from ARPES at

20 K [see Fig. 3(d)], the mobility is  $2.3$  cm<sup>2</sup>/(V s), in excellent agreement. We will discuss the temperature evolution of the MDC below.

Continuing the analysis, the Z-pocket mobility is  $4.3$  cm<sup>2</sup>/(V s) at 20 K. At lower temperatures, by extrapolating the  $T^2$  behavior to the zero-temperature limit, we find an improvement of mobility of  $29.1$  and  $26.9$  cm<sup>2</sup>/(V s), for the 2D-like Fermi surface and the Z pocket, respectively. We note that this two-channel model does not capture differences between the  $a$ - and  $b$ -axis resistivities since we have assumed that the quasi-2D channel is isotropic in the  $ab$  plane. Further corrections to the two-channel model, capturing this anisotropy difference, can be made by adding corrugations of the 2D-Fermi surface along the  $c$ -axis direction or the anisotropy of the Z pocket. We await future ARPES studies estimating the anisotropy of the Z pocket in all three directions and the quasiparticle lifetime along the Te-chain  $b$  direction to resolve this.

Next, we discuss the temperature dependence of the resistivities, focusing on three regimes. Although resistivities for all three axes undergo a large drop upon cooling to low temperatures, there is a qualitatively distinct temperature dependence between  $c$ -axis transport and that in the  $a$ - $b$  plane. As shown in Fig. 2, the resistivities start from a relatively high magnitude and drop rapidly below  $\sim 50$  K or less, with a qualitative difference found in  $\rho_c$ , which drops at lower temperatures than the other two components. Particularly in the intermediate-temperature regime, where the behavior of

$\rho(T)$  is richest, we compare with the temperature-dependent ARPES data.

*High temperature* ( $50\text{ K} \lesssim T \lesssim 300\text{ K}$ ). At high temperatures, the most apparent contrast in resistivity behavior is in the metalliclike ( $d\rho/dT < 0$ ) vs nonmetalliclike ( $d\rho/dT > 0$ ) behavior of  $\rho_c$  vs  $\rho_a$  and  $\rho_b$ , respectively. The weak increase of  $\rho_a$  and  $\rho_b$  upon cooling is attributed to single-ion Kondo behavior preceding the development of lattice coherence (although extracting a Kondo temperature is problematic due to its weak behavior, as detailed in SM [29] Sec. III). In contrast,  $\rho_c$  instead exhibits a metalliclike decrease on cooling. While definitely not Kondo-like, its weak temperature dependence also suggests that it is not simply a linear behavior due to electron-phonon scattering, suggesting that a single scattering mechanism may not be dominating. We note also that all three resistivities in this temperature window are larger than  $0.3\text{ m}\Omega\text{ cm}$ , which for typical metals is approaching the Anderson localization regime [33] as well as the Ioffe-Regel criterion for a highly anisotropic system (see SM [29] Sec. III for more details), but point to the lack of any obvious hopping conduction to rule out this scenario.

*Intermediate temperature* ( $5\text{ K} \lesssim T \lesssim 50\text{ K}$ ). In the intermediate-temperature regime, the richest qualitative anisotropy is apparent in the temperature range of  $\sim 50\text{ K}$ , where  $\rho_a$  and  $\rho_b$  exhibit the classic drop in magnitude upon the onset of Kondo coherence, while  $\rho_c$  begins to *increase* upon cooling, rising to a peak at  $14\text{ K}$  before dropping precipitously. In the following, we compare the temperature dependence of resistivity with that of ARPES spectra, finding consistency with a Kondo lattice coherence picture for  $a$ - $b$  plane transport, and investigate magnetotransport and magnetization data to help elucidate the  $c$ -axis behavior.

Figure 3 presents an analysis of ARPES temperature dependence, with a representative spectrum along the  $\Gamma$ - $X$  axis shown in Fig. 3(a). Integrating the region where dispersive bands are absent, we study the temperature dependence of the quasielastically scattered photoelectrons, as shown in Fig. 3(b). The peak within  $0.1\text{ eV}$  of the Fermi level, which is cut by the resolution-convoluted Fermi function, follows a typical temperature evolution as coherence develops. As shown in the inset of Fig. 3(b), tracking the peak magnitude as a function of temperature, an inflection can be seen around  $50\text{ K}$ , where  $\rho_a$  and  $\rho_b$  rapidly drop. This is consistent with the formation of Kondo coherence near  $50\text{ K}$ .

To make further connection to transport, we focus on energies close to the Fermi energy (ideally,  $E - E_F \lesssim k_B T$ ; however, this energy window is not adequately resolved in the measurement, so we use the closest available energy that can be analyzed). From the MDCs at  $25\text{ meV}$  binding energy, we find the width of the Lorentzian fits (feature width) to be changing with temperature, as shown in Fig. 3(d). Note that the fitting uncertainty is greater at higher temperatures due to irregular background intensity (see SM [29] Sec. VII for more details). We can interpret that the temperature dependence of the ARPES feature width and the electrical resistivity is mainly governed by the temperature dependence of the mean free path of the carriers. The key finding is that the temperature evolution of the ARPES  $6d$  band feature width, as shown in Fig. 3(d), is qualitatively consistent with the steadily decreasing behavior of  $\rho_a$  and  $\rho_b$  on cooling below the Kondo

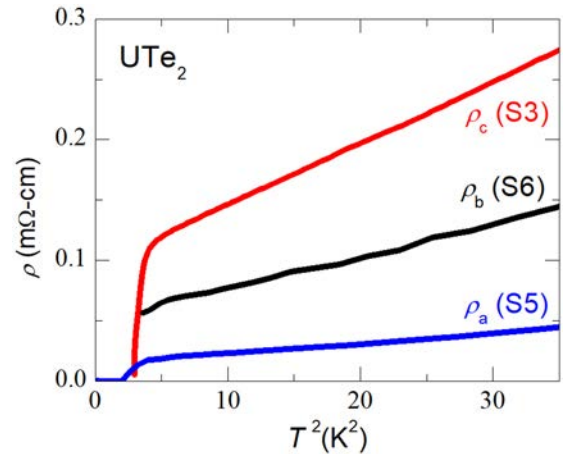


FIG. 4. Low-temperature resistivity of  $\text{UTe}_2$ , exhibiting Fermi liquid behavior for all three crystallographic orientations. Data were obtained from four-wire measurements on bar-shaped samples (samples S3, S5, and S6).

coherence temperature and inconsistent with the rising behavior of  $\rho_c$  in the same temperature range. Taken together with the behavior of the quasielastically scattered photoelectrons, this confirms the connection between the Kondo mechanism and  $a$ - $b$  plane resistivity and the anomalous distinction of  $c$ -axis transport.

Interestingly, the existence of an unusual qualitative anisotropy in resistivity temperature dependence has been observed in other systems such as  $\text{UCoGe}$  [34] and is a well-known phenomenon in highly two-dimensional metals such as  $\text{Sr}_2\text{RuO}_4$  [32] and cuprates, where its origin is still highly debated [35]. In contrast to the two-dimensionally anisotropic systems,  $c$ -axis transport in  $\text{UTe}_2$  is nearly equivalent in magnitude to its  $b$ -axis counterpart in this regime, suggesting that other qualitative anisotropic scattering mechanisms must be at play. Further below, we discuss an analysis of magnetotransport and magnetization that suggests magnetism is responsible.

*Low temperature* ( $T_c < T \lesssim 5\text{ K}$ ). Upon cooling, it is not clear how the two-channel model discussed above evolves below the rich anisotropic features at intermediate temperatures, but all three resistivities indicate the realization of a heavy-Fermi-liquid-like state at low temperatures, decreasing substantially and approaching a saturating behavior with a  $T^2$  dependence as shown in Fig. 4. (Note that bar-shaped samples are used for this analysis, using only sample data that agree with our generalized Montgomery technique measurements.) This is surprising, in light of experimental evidence for strong spin fluctuations [2] and quantum critical scaling [1], often associated with anomalous (i.e., non-Fermi liquid) scattering behavior. The  $T^2$  coefficient  $A$ , which is considered a measure of the strength of electron-electron interactions, is indeed enhanced in  $\text{UTe}_2$  as expected from the moderately large electronic density of states observed in the heat capacity [1], with values of  $0.76$ ,  $2.56$ , and  $5.03\ \mu\Omega\text{ cm/K}^2$  for  $\rho_a$ ,  $\rho_b$ , and  $\rho_c$ , respectively. The fact that all three coefficients are enhanced suggests that, however the band structure evolves through hybridization, all three conductivity components

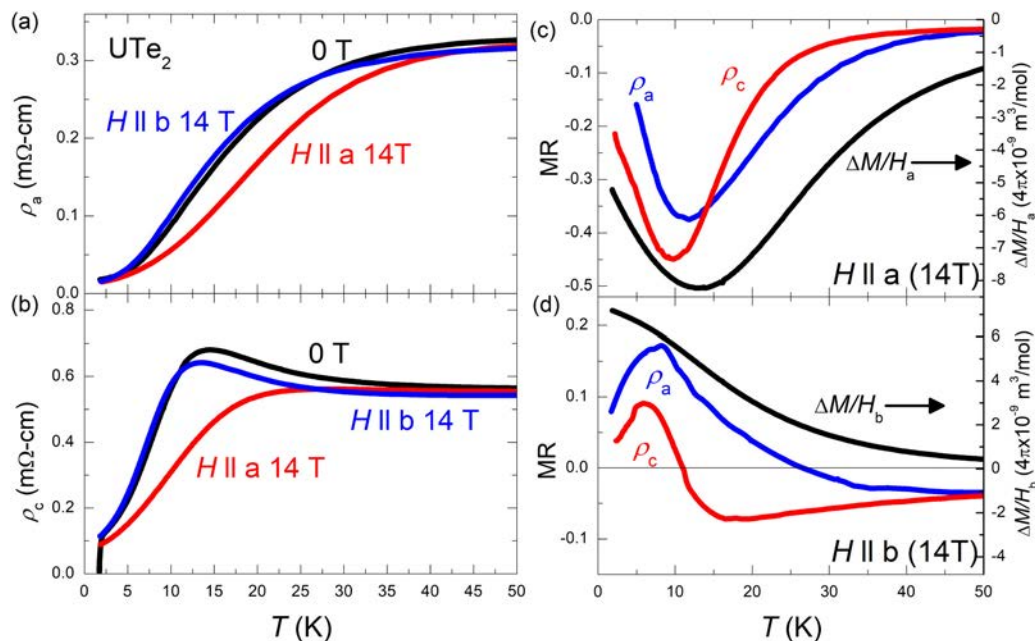


FIG. 5. Magnetotransport results at 14 T. (a)  $\rho_a$  vs temperature for both fixed at 0 T (in black),  $H \parallel a$  at 14 T (in red), and  $H \parallel b$  at 14 T (in blue). Data were taken using bar-shaped sample S7. (b)  $\rho_c$  vs temperature for both fixed at 0 T (in black),  $H \parallel a$  at 14 T (in red), and  $H \parallel b$  at 14 T (in blue). Data were taken using bar-shaped sample S3. (c) MR vs temperature and  $\Delta M/H_a$ . Field is applied along the  $a$ -axis direction. (d) MR vs temperature and  $\Delta M/H_b$ . Field is applied along the  $b$ -axis direction. Comparison of magnetoresistance for both  $\rho_a$  and  $\rho_c$  samples and  $\Delta M/H$ . Magnetoresistance (MR) is defined as  $\text{MR} = [\rho(14 \text{ T}) - \rho(0 \text{ T})]/\rho(0 \text{ T})$  and  $\Delta M/H = \chi_{\text{CW}} - M/H(14 \text{ T})$ , where  $\chi_{\text{CW}}$  is the Curie-Weiss susceptibility fitted at high temperatures.

entail heavy band characteristics. Furthermore, with the heaviest component along the  $c$  axis (by a factor of 6.6 as compared with  $\rho_a$ ), the anisotropy also evolves strongly as compared with a factor of  $\sim 3$  between the  $c$ - and  $a$ -axis resistivities at 20 K. Lower-temperature ARPES experiments will help shed light on this evolution.

**Magnetotransport.** To investigate the nature of the  $c$ -axis peak, we use field-orientation-dependent magnetoresistance (MR) as a probe of scattering anisotropy, focusing on whether MR exhibits a dependence on current or field direction. In UTe<sub>2</sub>, uranium atoms form chains along the magnetic easy axis ( $a$  axis), with nearest-neighbor ions forming ladder rungs parallel to the  $c$  axis. We therefore compare the response of  $\rho_a$  and  $\rho_c$  MR with fields applied both parallel ( $H \parallel a$ ) and perpendicular ( $H \parallel b$ ) to the uranium chains (other field orientations are presented in SM [29] Sec. V), expecting an anisotropic current response similar to the temperature dependence. Surprisingly, we find a nearly isotropic suppression of resistivity (i.e., negative MR) for both  $\rho_a$  and  $\rho_c$  with fields applied along the magnetic easy axis ( $a$  axis). As shown in Fig. 5, a negative MR is observed with  $H \parallel a$  for both resistivities up to Kondo coherence, not only, notably, for the peak in  $\rho_c$ , but also for the broad inflection in  $\rho_a(T)$ . For  $H \parallel b$ , both  $\rho_a$  and  $\rho_c$  exhibit a small positive MR at the lowest temperatures with a crossover on warming. As shown in Figs. 5(c) and 5(d), the normalized MR shows this comparison more clearly, suggesting that the MR response does not depend heavily on the current direction, but rather mostly on the magnetic field orientation. Similar results have been obtained for UCoGe and ascribed to magnetic fluctuations [36]. Together with other reported observations, we take these results as evidence for

the  $c$ -axis peak originating from a change in the magnetic spectrum.

An important reference is the magnetization at high fields. A Curie-Weiss (CW) susceptibility behavior,  $M/H = \chi_{\text{CW}}$ , was observed in UTe<sub>2</sub> at high temperatures for all three field orientations [1], consistent with the behavior of a Kondo lattice system above its coherence temperature. However, at lower temperatures, deviations from CW behavior occur, with  $M/H$  showing a maximum near 35 K for  $H \parallel b$  and an inflection point near 10 K for  $H \parallel a$  [1], with both features persisting to higher fields (see SM [29] Sec. V for all field orientations and different magnitudes). These features are comparable to those observed in our MR data. To emphasize this, we compare MR to the deviation of susceptibility from the CW behavior by plotting the difference ( $\Delta M/H = \chi_{\text{CW}} - M/H$ ) for both  $a$ - and  $b$ -axis directions, shown in Figs. 5(c) and 5(d). We do this analysis for two reasons. First, this subtraction emphasizes the subleading-order temperature dependence that only shows up as a mild slope change in the raw  $M/H$  data. Second, the sign of  $\Delta M/H$  indicates whether the susceptibility is changing faster or slower than the high-temperature CW behavior. For example, the CW behavior will saturate near the coherence temperature of a standard Kondo lattice, and therefore  $\Delta M/H$  will be positive. For  $H \parallel b$ , we find that  $\Delta M/H$  is indeed positive, but in contrast we find that  $\Delta M/H$  is negative for  $H \parallel a$ . The maximum in  $b$ -axis magnetization (i.e.,  $\Delta M/H > 0$ ) that occurs near the onset of Kondo coherence has been associated with an energy scale from the metamagnetic transition at 35 T [37,38], while the inflection in  $a$ -axis magnetization near 10 K (i.e.,  $\Delta M/H < 0$ ) appears to be dominated by easy-axis magnetism of the uranium chains

[1]. Interestingly, the comparison of MR and  $\Delta M/H$  reveals a qualitative similarity in both the temperature trend and sign for both field orientations, especially the  $\sim 10$  K negative peak feature for  $H \parallel a$ . This suggests that the change in scattering responsible for magnetotransport is predominantly magnetic in nature for both current directions.

Overall, the qualitative and quantitative differences observed between  $a$ - $b$  plane and  $c$ -axis transport, as well as the crossovers in resistivity anisotropy as a function of temperature, suggest that (1) at least two different transport channels are responsible for transport in different directions and (2) the scattering mechanism(s) involves energy scales that are quite sensitive to the temperature range under study. In addition, from magnetotransport studies, (3) the peak in  $\rho_c$  and minima in MR and  $\Delta M/H$  for  $H \parallel a$  occur at nearly the same temperature,  $\sim 10$  K, which is quite different from the Kondo coherence temperature observed in  $\rho_a$  and  $\rho_b$  in Fig. 2. All of these observations can be explained by a scattering mechanism with a distinct  $\sim 10$ -K energy scale that is magnetic (non-Kondo-like) in nature. For instance, this temperature is very close to the onset of quantum critical scaling of magnetization, with  $M/T \propto H/T^{1.5}$  [1], suggesting that it coincides with a change in the fluctuation spectrum, while high-temperature Curie-Weiss behavior indicates that antiferromagnetic interactions cannot be ignored. Details about the magnetic excitation spectrum are emerging [13–15,39] but may be challenging to interpret in a simple spin fluctuation picture due to the evolving heavy-fermion band structure [16]. Interestingly, nuclear magnetic resonance experiments [40,41] have revealed a divergence in the spin-spin relaxation rate  $1/T_2$  only for  $H \parallel a$ , also suggesting the development of spin fluctuations below  $\sim 20$  K and proximity to a (quasi) long-range ordered phase. In addition, given the absence of long-range magnetic order [2], the temperature scales observed in  $\rho_c(T)$ , the MR, and the magnetic response suggest a magnetic crossover scale that dominates the  $c$ -axis transport channel.

This work provides a definitive measure of the electrical resistivity along all three primary axes of  $\text{UTe}_2$  in the normal state. Given the expectation of strong anisotropy from electronic structure calculations, the magnitude of the  $c$ -axis resistivity is surprisingly comparable to that of the  $a$ - and  $b$ -axis resistivities in the entire temperature range but exhibits a qualitative difference in behavior at temperatures below the onset of Kondo coherence. We understand this behavior as originating from electronic bands with distinct dimensionality, as well as a scattering mechanism that is intimately tied to a crossover in the magnetic spectrum near 15 K. Adding valuable information to our understanding of the normal state of  $\text{UTe}_2$ , this information will be important for understanding the electronic structure and for building a microscopic theory of superconductivity.

#### ACKNOWLEDGMENTS

We thank D. Agterberg, I. Hayes, Y. Furukawa, Q. P. Ding, and C. Kurdak for inspiring discussions. Research at the University of Maryland was supported by Department of Energy Award No. DE-SC-0019154 (transport experiments), National Science Foundation Division of Materials Research Award No. DMR-1905891 (support of J.C.), the Gordon and Betty Moore Foundation's EPIQS Initiative through Grant No. GBMF9071 (materials synthesis), NIST, and the Maryland Quantum Materials Center. M.S.F. acknowledges support from the ARC Centre of Excellence in Future Low-Energy Electronics Technologies (FLEET, CE170100039). A.H.N. was supported by National Science Foundation Division of Materials Research Award No. DMR-1917511 and by Robert A. Welch Foundation Grant No. C-1818. This research used resources of the Advanced Light Source, a U.S. DOE Office of Science User Facility under Contract No. DE-AC02-05CH11231. Research at New York University was supported by the National Science Foundation under Grant No. DMR-2105081.

- 
- [1] S. Ran, C. Eckberg, Q.-P. Ding, Y. Furukawa, T. Metz, S. R. Saha, I.-L. Liu, M. Zic, H. Kim, J. Paglione, and N. P. Butch, *Science* **365**, 684 (2019).
- [2] S. Sundar, S. Gheidi, K. Akintola, A. M. Cote, S. R. Dunsiger, S. Ran, N. P. Butch, S. R. Saha, J. Paglione, and J. E. Sonier, *Phys. Rev. B* **100**, 140502(R) (2019).
- [3] T. Metz, S. Bae, S. Ran, I. Lin Liu, Y. S. Eo, W. T. Fuhrman, D. F. Agterberg, S. M. Anlage, N. P. Butch, and J. Paglione, *Phys. Rev. B* **100**, 220504(R) (2019).
- [4] G. Nakamine, S. Kitagawa, K. Ishida, Y. Tokunaga, H. Sakai, S. Kambe, A. Nakamura, Y. Shimizu, Y. Homma, D. Li, F. Honda, and D. Aoki, *J. Phys. Soc. Jpn.* **88**, 113703 (2019).
- [5] S. Ran, I.-L. Liu, Y. S. Eo, D. J. Campbell, P. M. Neves, W. T. Fuhrman, S. R. Saha, C. Eckberg, H. Kim, D. Graf, F. Balakirev, J. Singleton, J. Paglione, and N. P. Butch, *Nat. Phys.* **15**, 1250 (2019).
- [6] G. Knebel, W. Knafo, A. Pourret, Q. Niu, M. Vališka, D. Braithwaite, G. Lapertot, M. Nardone, A. Zitouni, S. Mishra, I. Sheikin, G. Seyfarth, J.-P. Brison, D. Aoki, and J. Flouquet, *J. Phys. Soc. Jpn.* **88**, 063707 (2019).
- [7] D. Braithwaite, M. Vališka, G. Knebel, G. Lapertot, J.-P. Brison, A. Pourret, M. Zhitomirsky, J. Flouquet, F. Honda, and D. Aoki, *Commun. Phys.* **2**, 147 (2019).
- [8] S. Ran, H. Kim, I. Lin Liu, S. R. Saha, I. Hayes, T. Metz, Y. S. Eo, J. Paglione, and N. P. Butch, *Phys. Rev. B* **101**, 140503(R) (2020).
- [9] I. M. Hayes, D. S. Wei, T. Metz, J. Zhang, Y. S. Eo, R. Ran, S. R. Saha, J. Collini, N. P. Butch, D. F. Agterberg, A. Kapitulnik, and J. Paglione, *Science* **373**, 797 (2021).
- [10] A. H. Nevidomskyy, *arXiv:2001.02699*.
- [11] L. Jiao, S. Howard, S. Ran, Z. Wang, J. O. Rodriguez, M. Sigrist, Z. Wang, N. P. Butch, and V. Madhavan, *Nature (London)* **579**, 523 (2020).
- [12] S. Bae, H. Kim, Y. S. Eo, S. Ran, I.-L. Liu, W. T. Fuhrman, J. Paglione, N. P. Butch, and S. M. Anlage, *Nat. Commun.* **12**, 2644 (2021).

- [13] C. Duan, K. Sasmal, M. B. Maple, A. Podlesnyak, J.-X. Zhu, Q. Si, and P. Dai, *Phys. Rev. Lett.* **125**, 237003 (2020).
- [14] W. Knafo, G. Knebel, P. Steffens, K. Kaneko, A. Rosuel, J.-P. Brison, J. Flouquet, D. Aoki, G. Lapertot, and S. Raymond, *Phys. Rev. B* **104**, L100409 (2021).
- [15] C. Duan, R. Baumbach, A. Podlesnyak, Y. Deng, C. Moir, A. J. Breindel, M. B. Maple, E. Nica, Q. Si, and P. Dai, *Nature (London)* **600**, 636 (2021).
- [16] N. P. Butch, S. Ran, S. R. Saha, P. M. Neves, M. P. Zic, J. Paglione, S. Gladchenko, Q. Ye, and J. A. Rodriguez-Rivera, *npj Quantum Mater.* **7**, 39 (2022).
- [17] S. M. Thomas, C. Stevens, F. B. Santos, S. S. Fender, E. D. Bauer, F. Ronning, J. D. Thompson, A. Huxley, and P. F. S. Rosa, *Phys. Rev. B* **104**, 224501 (2021).
- [18] P. F. Rosa, A. Weiland, S. S. Fender, B. L. Scott, F. Ronning, J. D. Thompson, E. D. Bauer, and S. M. Thomas, *Commun. Mater.* **3**, 33 (2022).
- [19] D. Aoki, J. Brison, J. Flouquet, K. Ishida, G. Knebel, Y. Tokunaga, and Y. Yanase, *J. Phys.: Condens. Matter* **34**, 243002 (2022).
- [20] L. Miao, S. Liu, Y. Xu, E. C. Kotta, C.-J. Kang, S. Ran, J. Paglione, G. Kotliar, N. P. Butch, J. D. Denlinger, and L. A. Wray, *Phys. Rev. Lett.* **124**, 076401 (2020).
- [21] W.-C. Lin, D. J. Campbell, S. Ran, I.-L. Liu, H. Kim, A. H. Nevidomskyy, D. Graf, N. P. Butch, and J. Paglione, *npj Quantum Mater.* **5**, 68 (2020).
- [22] Q. Niu, G. Knebel, D. Braithwaite, D. Aoki, G. Lapertot, G. Seyfarth, J. P. Brison, J. Flouquet, and A. Pourret, *Phys. Rev. Lett.* **124**, 086601 (2020).
- [23] Q. Niu, G. Knebel, D. Braithwaite, D. Aoki, G. Lapertot, M. Vališka, G. Seyfarth, W. Knafo, T. Helm, J.-P. Brison, J. Flouquet, and A. Pourret, *Phys. Rev. Research* **2**, 033179 (2020).
- [24] S. Thomas, F. Santos, M. Christensen, T. Asaba, F. Ronning, J. Thompson, E. Bauer, R. Fernandes, G. Fabbris, and P. Rosa, *Sci. Adv.* **6**, eabc8709 (2020).
- [25] D. Aoki, A. Nakamura, F. Honda, D. Li, Y. Homma, Y. Shimizu, Y. J. Sato, G. Knebel, J.-P. Brison, A. Pourret, D. Braithwaite, G. Lapertot, Q. Niu, M. Vališka, H. Harima, and J. Flouquet, *J. Phys. Soc. Jpn.* **88**, 043702 (2019).
- [26] S.-i. Fujimori, I. Kawasaki, Y. Takeda, H. Yamagami, A. Nakamura, Y. Homma, and D. Aoki, *J. Phys. Soc. Jpn.* **88**, 103701 (2019).
- [27] A. B. Shick and W. E. Pickett, *Phys. Rev. B* **100**, 134502 (2019).
- [28] J. Ishizuka, S. Sumita, A. Daido, and Y. Yanase, *Phys. Rev. Lett.* **123**, 217001 (2019).
- [29] See Supplemental Material at <https://link.aps.org/supplemental/10.1103/PhysRevB.106.L060505> for details regarding experimental design, analysis, fitting, and ARPES measurements, which includes Refs. [42–50].
- [30] H. Montgomery, *J. Appl. Phys.* **42**, 2971 (1971).
- [31] M. A. Tanatar, N. Ni, C. Martin, R. T. Gordon, H. Kim, V. G. Kogan, G. D. Samolyuk, S. L. Bud'ko, P. C. Canfield, and R. Prozorov, *Phys. Rev. B* **79**, 094507 (2009).
- [32] N. E. Hussey, A. P. Mackenzie, J. R. Cooper, Y. Maeno, S. Nishizaki, and T. Fujita, *Phys. Rev. B* **57**, 5505 (1998).
- [33] Y. Imry, *Introduction to Mesoscopic Physics* (Oxford University Press, Oxford, 2002).
- [34] T. Hattori, Y. Ihara, Y. Nakai, K. Ishida, Y. Tada, S. Fujimoto, N. Kawakami, E. Osaki, K. Deguchi, N. K. Sato, and I. Satoh, *Phys. Rev. Lett.* **108**, 066403 (2012).
- [35] D. B. Gutman and D. L. Maslov, *Phys. Rev. Lett.* **99**, 196602 (2007).
- [36] M. Taupin, L. Howald, D. Aoki, J. Flouquet, and J. P. Brison, *Phys. Rev. B* **89**, 041108(R) (2014).
- [37] A. Miyake, Y. Shimizu, Y. J. Sato, D. Li, A. Nakamura, Y. Homma, F. Honda, J. Flouquet, M. Tokunaga, and D. Aoki, *J. Phys. Soc. Jpn.* **88**, 063706 (2019).
- [38] K. Miyake, *J. Phys. Soc. Jpn.* **90**, 024701 (2021).
- [39] K. Willa, F. Hardy, D. Aoki, D. Li, P. Wiecki, G. Lapertot, and C. Meingast, *Phys. Rev. B* **104**, 205107 (2021).
- [40] Y. Tokunaga, H. Sakai, S. Kambe, T. Hattori, N. Higa, G. Nakamine, S. Kitagawa, K. Ishida, A. Nakamura, Y. Shimizu, Y. Homma, D. Li, F. Honda, and D. Aoki, *J. Phys. Soc. Jpn.* **88**, 073701 (2019).
- [41] Y. Tokunaga, H. Sakai, S. Kambe, Y. Haga, Y. Tokiwa, P. Opletal, H. Fujibayashi, K. Kinjo, S. Kitagawa, K. Ishida, A. Nakamura, Y. Shimizu, Y. Homma, D. Li, F. Honda, and D. Aoki, *J. Phys. Soc. Jpn.* **91**, 023707 (2022).
- [42] C. A. M. dos Santos, A. De Campos, M. Da Luz, B. White, J. Neumeier, B. De Lima, and C. Shigue, *J. Appl. Phys.* **110**, 083703 (2011).
- [43] I. Miccoli, F. Edler, H. Pfnür, and C. Tegenkamp, *J. Phys.: Condens. Matter* **27**, 223201 (2015).
- [44] T. Costi, A. Hewson, and V. Zlatic, *J. Phys.: Condens. Matter* **6**, 2519 (1994).
- [45] A. Zabrodski, *Philos. Mag. B* **81**, 1131 (2001).
- [46] D. A. Shirley, *Phys. Rev. B* **5**, 4709 (1972).
- [47] M. Lee, J. R. Williams, S. Zhang, C. D. Frisbie, and D. Goldhaber-Gordon, *Phys. Rev. Lett.* **107**, 256601 (2011).
- [48] Y. S. Eo, K. Sun, C. Kurdak, D.-J. Kim, and Z. Fisk, *Phys. Rev. Applied* **9**, 044006 (2018).
- [49] N. Andrei, K. Furuya, and J. Lowenstein, *Rev. Mod. Phys.* **55**, 331 (1983).
- [50] J. Parks, A. Champagne, T. Costi, W. Shum, A. Pasupathy, E. Neuscamman, S. Flores-Torres, P. Cornaglia, A. Aligia, C. Balseiro, G. K.-L. Chan, H. D. Abruña, and D. C. Ralph, *Science* **328**, 1370 (2010).

**Supplementary Material:**  
**c-axis Transport in UTe<sub>2</sub>: Evidence of Three Dimensional  
Conductivity Component**

Yun Suk Eo,<sup>1</sup> Shouzheng Liu,<sup>2</sup> Shanta R. Saha,<sup>1</sup> Hyunsoo Kim,<sup>1,\*</sup> Sheng Ran,<sup>1,3</sup>  
Jarryd A. Horn,<sup>1</sup> Halyna Hodovanets,<sup>1,\*</sup> John Collini,<sup>1</sup> Tristin Metz,<sup>1</sup> Wesley  
T. Fuhrman,<sup>1</sup> Andriy H. Nevidomskyy,<sup>4</sup> Jonathan D. Denlinger,<sup>5</sup> Nicholas P.  
Butch,<sup>1,3</sup> Michael S. Fuhrer,<sup>6,7</sup> L. Andrew Wray,<sup>2</sup> and Johnpierre Paglione<sup>1,8</sup>

<sup>1</sup>*Maryland Quantum Materials Center and Department of Physics,  
University of Maryland, College Park, Maryland, USA*

<sup>2</sup>*Department of Physics, New York University, New York, New York, USA*

<sup>3</sup>*NIST Center for Neutron Research,  
National Institute of Standards and Technology, Gaithersburg, MD 20899, USA*

<sup>4</sup>*Department of Physics and Astronomy,  
Rice University, Houston, Texas 77005, USA*

<sup>5</sup>*Advanced Light Source, Lawrence Berkeley National Laboratory, Berkeley, CA 94720, USA*

<sup>6</sup>*Monash University, Melbourne, Victoria 3800, Australia*

<sup>7</sup>*ARC Centre of Excellence in Future Low-Energy Electronics Technologies,  
Monash University, Victoria 3800 Australia*

<sup>8</sup>*Canadian Institute for Advanced Research,  
Toronto, Ontario M5G 1Z8, Canada<sup>†</sup>*

(Dated: August 4, 2022)

## CONTENTS

I. Experimental Design	2
A. $\text{UTe}_2$ Crystal Growth	2
B. Difficulty Estimating the c-axis Resistivity	3
C. Preparation of the Electrodes	3
D. Sample Geometry	4
E. Generalized Montgomery geometry	5
II. Experimental Analysis	8
A. Resistivity Result	8
B. Comparison of Numerical vs. Montgomery formula for Sample S2	11
III. Fitting the Temperature Dependence of Resistivity at High Temperatures	12
IV. Magnetization Analysis	15
V. Magnetotransport Analysis	17
VI. Transport and ARPES Comparison	18
VII. ARPES Measurements and Fitting	20
References	22

### I. EXPERIMENTAL DESIGN

#### A. $\text{UTe}_2$ Crystal Growth

Single crystals were grown identical to the method used in our previous studies such as Ref. [1] and Ref. [2].  $\text{UTe}_2$  crystals were grown by chemical vapor transport technique. Iodine was used for the transport agent. Elements of uranium and tellurium were prepared with a 2:3 atomic ratio in the quartz tube with the iodine of  $3 \text{ mg/cm}^3$ . This quartz ampoule was gradually heated in the furnace and then a temperature gradient between 1060 C to 1000 C was maintained for 7 days. The furnace was then cooled to room temperature.

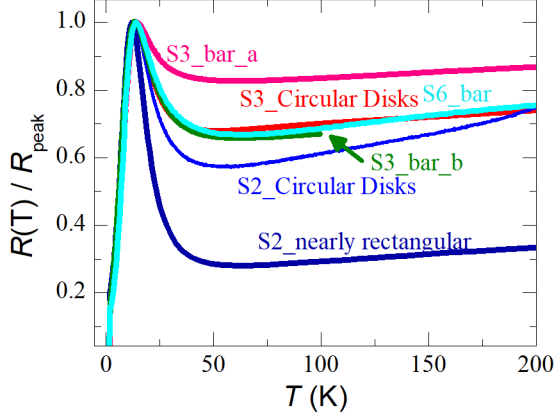


FIG. 1. (Color) Various attempts to measure the  $c$ -axis resistivity. The resistances are normalized with the value at the peak that is located 12-14 K. Note that identical samples show different behavior above the peak temperature when the geometry is different. The "Circular Disks" sample has an inner radius is  $170 \mu\text{m}$ , outer radius is  $270 \mu\text{m}$ , and the thickness is  $435 \mu\text{m}$ .

### B. Difficulty Estimating the $c$ -axis Resistivity

In Fig. 1, we show some of our early attempts for finding  $\rho_c$ . The data is normalized to the resistance at the peak, particularly two samples that are also presented in this work. The plots that are labeled 'bar' are from standard four wire measurements on a bar-shaped sample. The plots that are labeled 'Circular Disks' are electric current flowing through the  $c$ -axis by two circular disks patterned on opposite  $ab$  planes. The plot labeled 'nearly rectangular' is a resistance measurement from electrodes placed at the corners of a nearly rectangular sample (same as  $R_1$  configuration in Fig. (3)). In this figure, we see that even for identical samples, the resistance enhancement from the peak to high temperatures depends on the geometry of the sample and the position of the electrodes. From this, one can see that finding  $\rho_c$  accurately is difficult.

### C. Preparation of the Electrodes

Preparing reliable contacts for resistivity measurements of  $\text{UTe}_2$  is difficult. If the electrodes are prepared by using silver paste or silver epoxy on a fresh surface of  $\text{UTe}_2$ , two-terminal resistance values (mainly contact resistances of the two electrodes) easily degrade

from a couple of  $\Omega$ s to a  $100\text{k}\Omega$  -  $\text{M}\Omega$  range within hours of exposure to ambient conditions. This is most likely because the native oxide layer forms rapidly on the surface. One alternative strategy is putting highly conductive metal contacts (e.g. gold or silver) by lithographic methods. Since this also requires a rapid preparation before the sample is inserted into the vacuum chamber of the metal evaporator, it is difficult to convince that the metal pattern is touching the sample surface uniformly. To the best of our knowledge, we find soldered contacts provide the smallest contact resistance that is stable for many hours during exposure to ambient conditions. However, soldered contacts are difficult to define precise electrode geometries. To avoid this complication, we put contacts on the edges as small as possible, similar to a Van der Pauw or Montgomery geometry. The contacts are first made by alloys of indium solder as small as possible, and the wires were connected by silver paste on top of the solder for better controllability. This ensures that the contact size can only be smaller than the visible contact but not larger. All two-terminal resistance values were in the several  $0.1 - 1 \Omega$  Ohmic range so that the distortion of the voltage signal by common-mode from the preamplifier is not an issue for measuring the normal state resistance of  $\text{UTe}_2$ .

#### D. Sample Geometry

For sample S1, the top and bottom surfaces are  $bc$  planes. The edges of this sample are all created by natural cleavage, and directions are diagonal to  $\pm\vec{b}$ - and  $\pm\vec{c}$ -direction (e.g.,  $\vec{b} \pm \vec{c}$ ), as shown in Fig. 3 (a). For sample S2, we prepared a Montgomery-like sample where the top and bottom surface shapes are nearly rectangular. The top and bottom surfaces are  $ac$  planes by polishing as shown in Fig. 3 (b). This sample was polished in all six directions. If the samples are sufficiently thin, a resistance measurement in sample S1 would depend on the resistivity of  $c$  ( $\rho_c$ ) and  $b$  ( $\rho_b$ ), and sample S2 would depend on the resistivity of  $c$  ( $\rho_c$ ) and  $a$  ( $\rho_a$ ). As shown in Fig. 2, magnetization measurements along the field direction where  $a$ -,  $b$ - and  $c$ -axis is predicted from those edges are consistent with the previous report in terms of shape and magnitude[1].

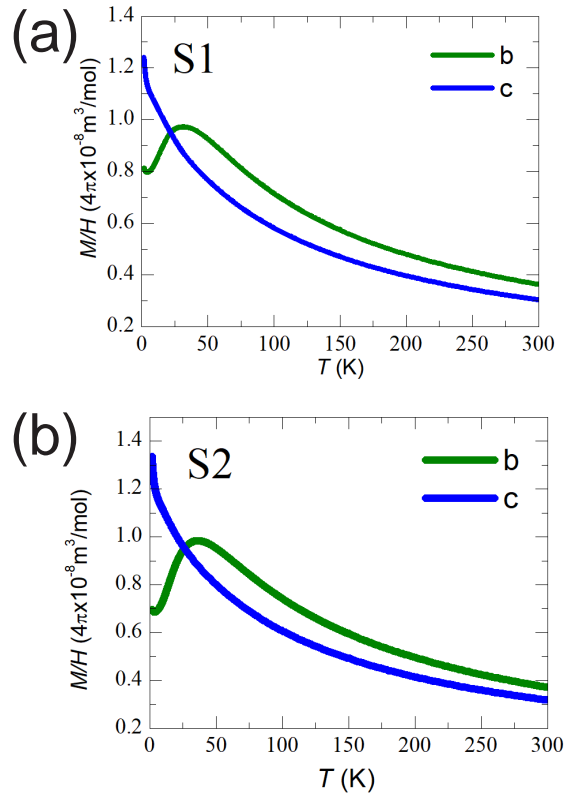


FIG. 2. (Color) Measurement of magnetization. The samples are mounted along the field directions indicated in the arrows of Fig. 3. (a) Sample S1. (b) Sample S2.

### E. Generalized Montgomery geometry

The Montgomery method[3] is a standard method for finding the anisotropy of the conductivities when the sample is prepared as a perfect rectangular shape, where the edges are exactly aligned with the crystallographic axes[3, 4].

Today, thanks to the improved computing power, irregular-shaped geometries can be simulated easier than before. Still, although numerical calculations can find the resistance values of a given set of conductivity tensor components for a given geometry, the opposite task (finding the conductivity tensor components from a set of resistance values) is challenging. We introduce a scaling formalism[5] for two conductivity tensor components.

Consider a simple case where the conductivities in all three directions are identical to  $\sigma$  (e.g., cubic crystal). The resistance is inversely related to  $\sigma$ , and therefore

$$R = C/\sigma t, \quad (1)$$

where  $C$  is a constant that depends on the transport geometry and electrode positions, and  $t$  is the thickness. Although it is very obvious, notice that the  $R$  always scales with  $1/\sigma$ . Because of this relation, an experimentalist is often tempted to report the ratio of resistances at different conditions, such as temperature for example. This is because such relation, independent of the details of the measurement

$$\frac{R(T)}{R(T = 300K)} = \frac{\sigma(300K)}{\sigma(T)} \quad (2)$$

is justified.

For resistance of an anisotropic crystal, it can be calculated by integrating Ohm's law,  $J = \tilde{\sigma}E$  over the geometry of the sample with the appropriate boundary conditions, where

$$\tilde{\sigma} = \begin{pmatrix} \sigma_a & 0 & 0 \\ 0 & \sigma_b & 0 \\ 0 & 0 & \sigma_c \end{pmatrix}, \quad (3)$$

and  $\sigma_a$ ,  $\sigma_b$ , and  $\sigma_c$ , are the conductivities along the  $a$ -,  $b$ -, and  $c$ -axis of the crystal.

Resistance, in general, is then a function of all of these conductivities:

$$R = R(\sigma_a, \sigma_b, \sigma_c). \quad (4)$$

If the geometry is sufficiently thin in the  $c$ -axis direction, the resistance does not depend on  $\sigma_c$ . We can express resistance as:

$$R = r(\sigma_a, \sigma_b)/t. \quad (5)$$

The value of  $r(\sigma_a, \sigma_b)$  depends on the transport geometry and the position of the contacts in addition to  $\sigma_a$  and  $\sigma_b$ . In order to find two unknown conductivities,  $\sigma_a$  and  $\sigma_b$ , at least two independent resistance measurements, say  $R_1$  and  $R_2$ , from different configurations are required. As mentioned before, the difficulty is that unless an analytical form is known finding the conductivity by an inverse mapping of two parameters,  $(\sigma_a, \sigma_b) = (R_1^{-1}, R_2^{-1})$  requires a tedious work and heavy numerical computing. In addition, Eq. (1) cannot be assumed and therefore the resistance ratio  $(R(T)/R(T = 300K))$  may not be as useful unless the current is flowing only in one direction.

Still, a slightly less obvious scaling property than the isotropic  $\sigma$  case holds. This scaling property is useful for finding the unknown  $\sigma_a$  and  $\sigma_b$ . It can be easily convinced that Eq. (5) can be expressed alternatively as:

$$R = \frac{f(x = \sigma_a/\sigma_b)}{\sigma_b t}. \quad (6)$$

From Eq. (6), we have reformulated this problem of finding the conductivity ratio,  $x$  ( $= \sigma_a/\sigma_b$ ) and  $\sigma_b$  instead of finding  $\sigma_a$  and  $\sigma_b$ . We can first attempt to find  $x$ . For convenience, we take the ratio of the two resistances,  $R_1$  and  $R_2$ , and define  $g$  by

$$g(x) = \frac{R_1(x)}{R_2(x)} = \frac{f_1(x)}{f_2(x)}. \quad (7)$$

Numerical simulations can provide  $g(x)$  by an iterative process of varying  $x$ . we can later directly compare this with the experimental resistance ratio.

We summarize the procedure to find the two resistivities ( $\sigma_a$  and  $\sigma_b$ ) from two resistance measurements ( $R_1$  and  $R_2$ ).

- Step 1: From the experimental measurements of  $R_1(T)$  and  $R_2(T)$  values, calculate  $R_1(T)/R_2(T)$ . We define this quantity as  $g(T)^e$ .
- Step 2: From numerical simulations of  $f_1$  and  $f_2$ , we define the ratio of the two as  $g(x)^n$ .
- Step 3. From  $g(x)^n$  in Step 2, find the inverse function,  $x(g)^n$  for a wide range of  $g$  values. By definition, this is identical to finding  $\sigma_a/\sigma_b$  as a function of  $R_1/R_2$ .
- Step 4. Use the experimental values of  $R_1/R_2$  as a function of temperature from Step 1 to the numerically found  $x(g)^n$  (from Step 3) and find  $\sigma_a/\sigma_b$  as a function of temperature.
- Step 5. Since  $x(T)$  is found from Step 4, from Eq. (6), use  $f_1(x(T))$  and  $R_1(T)$  to find  $\sigma_b(T)$ . (Note: alternatively,  $f_2(x(T))$  and  $R_2(T)$  can be used).
- Step 6. Since  $\sigma_b(T)$  is found, compare this to  $x(T)$  from Step 3 and find  $\sigma_a(T)$ .

In the following section, we use this technique and extract the resistivities in all three directions.

## II. EXPERIMENTAL ANALYSIS

### A. Resistivity Result

In this section, we describe in detail how the resistivities in all three directions were found. Also, we discuss the validity of our analysis.

The samples are shown in the insets of Fig. (3) (a) and (b), with the electrodes labeled. we label the four-terminal resistance as  $V_{k,l}/I_{i,j}$ , where  $i, j, k$ , and  $l$  are the labels of the electrodes. A sample that consist of four electrodes can provide three independent four-terminal resistance measurements. Each resistance measurement,  $R_1$ ,  $R_2$ , and  $R_3$  are shown in Fig. (3) (a) for S1 and Fig. (3) (b) for S2. For both samples S1 and S2, we find that  $R_1$ ,  $R_2$ , and  $R_3$  have different temperature behaviors. This is because each resistance configuration sweeps the current and measures the voltage drop in different regions of the sample, emphasizing the two resistivity (or conductivity) components differently.

We use the scaling formalism to extract the resistivities from measured resistance. First, for the numerical simulations to be useful, we solve  $R_1$ ,  $R_2$ , and  $R_3$  with iterations of  $x$  ( $x = \sigma_b/\sigma_c$  for S1 and  $x = \sigma_a/\sigma_c$  for S2). The results are shown in Fig. 4 (a) (for S1) and (b) (for S2).

Interestingly, even before extracting the resistivities, by comparing the numerical results and the experimental resistance data at a glance, we find that the c-axis resistivity is comparable in magnitude to the other resistivities. At room temperature, for example, sample S1 is  $R_1 < R_2 < R_3$ , this implies that  $f_1 < f_2 < f_3$ . In Fig. (4) (a), the allowed range of  $x$  in this order is 0.4 - 4. This already tells us that the c-axis resistivity cannot be many orders of magnitude larger than the a-axis resistivity. Similar arguments can be made at different temperature ranges for both samples. Note that for S2,  $f_3$  changes sign at  $x \sim 2$  in Fig. (4) (b). Indeed,  $R_3$  changes sign at  $\sim 35$  K. This again indicates the c-axis resistivity is only about twice as large than the a-axis resistivity.

Our three measurements per sample provides a sanity check of our resistivity results. Ideally, since only two resistance measurements are required for the extraction of two resistivities, three resistance measurements provide resistivity extractions in three different ways ( $R_1$  and  $R_2$ ,  $R_1$  and  $R_3$ , or  $R_2$  and  $R_3$ ). The possible disagreement of the the three extracted resistivities would indicate the reliability (e.g., homogeneity of the sample or how

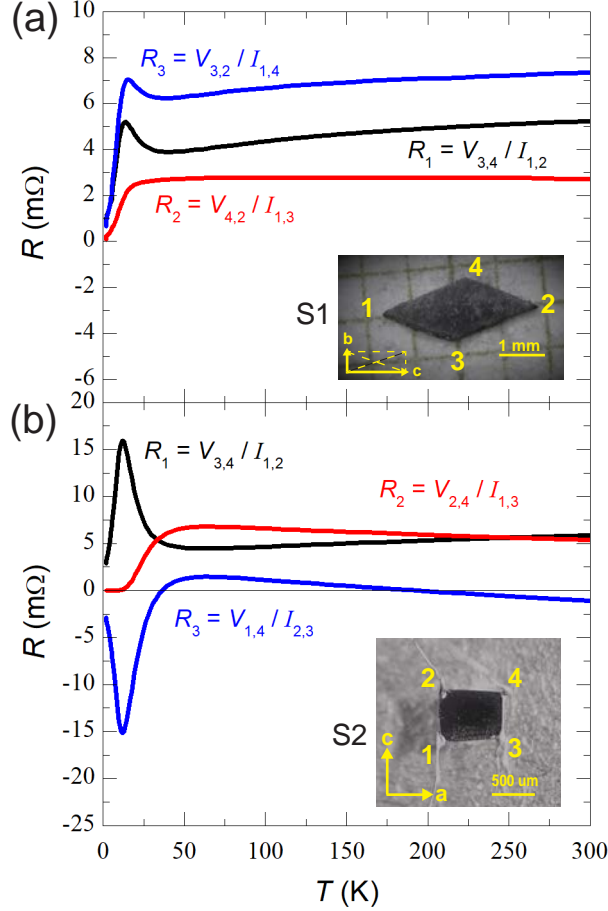


FIG. 3. (Color) Sample configuration and resistance vs. temperature from each configuration. (a) Resistance vs temperature of S1 sample for three different configurations. Inset: Sample S1 in the bc plane. Sample thickness is 290 microns. (b) Resistance vs temperature of S2 sample for three different configurations. Inset: Sample S2 in the ac plane. Sample thickness is 160 microns.

accurate the sample geometry information was used in numerical simulation) of this study. We plot  $\rho_a$  and  $\rho_b$  in Fig. (5) (c) and  $\rho_c$  in Fig. (5) (d), both from samples S1 and S2. The disagreement of the three different resistivity extractions are shown as an error bar (as error of mean) in each of the plots. From the size of the error bars, we believe the uniformity of the samples are good enough to represent the resistivities, including the absolute magnitude. Since we gain confidence from these two measurements from S1 and S2, we also plot together a  $\rho_c$  prepared as a bar-shaped sample (S3) that shows similar behavior as the previous sample results. The agreement especially between S3 and S2 is good once the data has been adjusted by 10 percent. We believe this difference is within the error of the contact

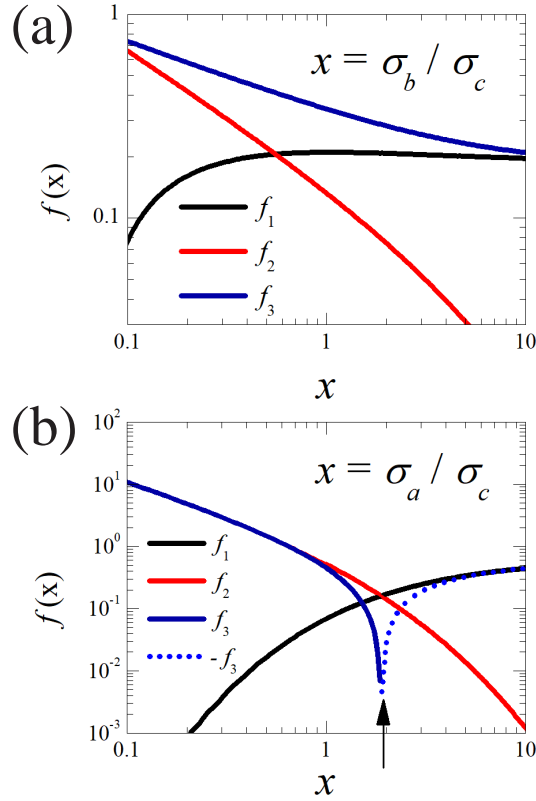


FIG. 4. (Color) Solving numerically  $f_1$ ,  $f_2$ , and  $f_3$  varying  $x$ . (a) For geometry S1 in the  $bc$  plane. (b) For geometry S2 in the  $ac$  plane. Note that  $f_2$  changes sign, as indicated with an arrow. The negative values are plotted as  $-f_2$  (dotted line).

position and sample dimension measurements.

One detail to note is that the slight variations of the  $\rho_c$  from S1 and S2 have a difference in slope at temperatures above the peak. Since the size of the error bars in  $\rho_c$  from S1 is smaller than that of S2, and also the misalignment from the true crystal axis and the edges of the geometry is more reliable in S1 since its edges are unpolished, we present  $\rho_c$  in the main text.

Note that the shape of S2 can be approximated as a rectangle. Assuming the sample shape is a perfect rectangle, we find the resistivities using the standard Montgomery formula in the following section. We find the resistivities are also in good agreement with the numerical extraction results.

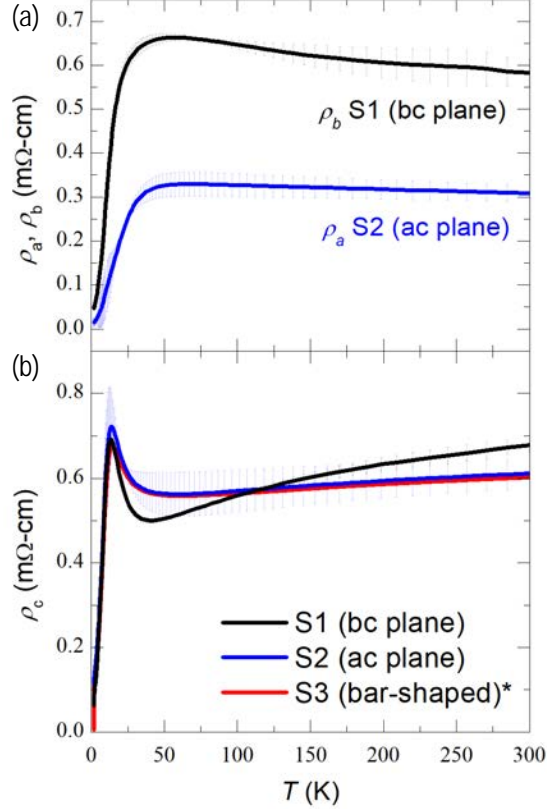


FIG. 5. Resistivity results from three samples. (a)  $\rho_a$  from sample S2 and  $\rho_b$  from sample S1. (b)  $\rho_c$  from sample S1, S2, and S3.\*The resistivity of S3 was adjusted by a 10% magnitude change (multiplied by 1.1) from the estimated geometric factor by length, width, and thickness. The error bars are error of mean among three different resistivity extraction results.

### B. Comparison of Numerical vs. Montgomery formula for Sample S2

Since sample S2 is roughly rectangular shape, it is worth to compare the resistivities found from numerical simulations with the resistivities estimated from the standard Montgomery formula.

As mentioned before, an analytical approximation is available for the Montgomery formula[4, 6]. Here, only  $R_1$  and  $R_2$  is used. If the length of the rectangular along the  $c$ -axis and  $a$ -axis is  $l'_c$  and  $l'_a$ , respectively, and the thickness is  $t$ , the resistivity along the  $c$ -axis is approximately[4, 6]

$$\rho_c \approx \frac{\pi}{8} \left( \frac{t l'_a}{l'_c} \right) \frac{l_c}{l_a} \sinh\left(\pi \frac{l_a}{l_c}\right), \quad (8)$$

where

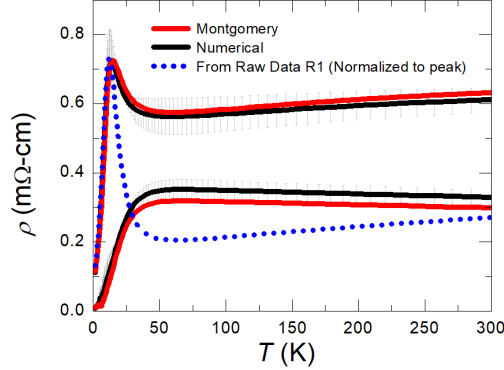


FIG. 6. (Color) Resistivity along the  $c$ -axis and  $a$ -axis from S1. The black lines are from numerical analysis. The red lines are from the Montgomery formula (using Eq. (8) and Eq. (9)).

$$\frac{l_a}{l_c} = \frac{1}{2} \left[ \frac{1}{\pi} \ln \frac{R_2}{R_1} + \sqrt{\left( \frac{1}{\pi} \ln \left( \frac{R_2}{R_1} \right) \right)^2 + 4} \right]. \quad (9)$$

Resistivity along the  $a$ -axis can be found trivially by interchanging  $l'_a$  and  $l'_c$ ,  $l_a$  and  $l_c$ , and  $R_1$  and  $R_2$ . We plot together the resistivity converted from numerical analysis and the Montgomery formula in Fig. 6. The results from two different methods provide a good agreement (black is from numerical analysis and red is from the Montgomery formula). This is another verification that our resistivity conversions are reliable. Lastly, we compare the  $c$ -axis resistivity result to  $R_1$ , normalized to the peak resistivity value. It is interesting to note that the raw data from  $R_1$  (in a blue dotted line) results in a larger resistance ratio ( $R(T = peak)/R(T = 300K)$ ) when compared to the room temperature value. However, our analysis shows that this is a result of a mixture of the higher conductivity along the  $a$ -axis.

### III. FITTING THE TEMPERATURE DEPENDENCE OF RESISTIVITY AT HIGH TEMPERATURES

In this subsection, we fit the high temperature region of resistivity, where the temperature dependence is  $d\rho/dT < 0$ . We first try fitting the Kondo scattering mechanism in the dilute limit (single-ion limit). We next consider the possibility of variable range hopping, which is expected in the localization regime. In short, we rule out the possibility of hopping conduction. The Kondo scattering mechanism can be a possible scenario, but the range of

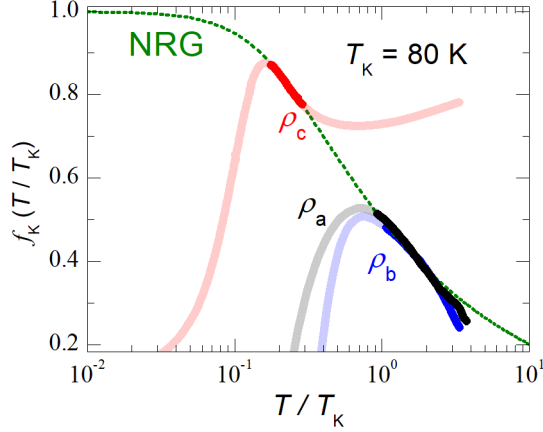


FIG. 7. (Color) Attempt of resistivities comparing with the numerical renormalization group (NRG) analysis. One can see that the range of fitting is small.

resistivity magnitude change is too small, and therefore we cannot find a reliable Kondo temperature.

### • Kondo Scattering

In a Kondo lattice at high temperatures, where coherence has not developed to form a Fermi liquid, we can think of the system as conduction electrons interacting with localized magnetic impurities. Therefore, we consider the functional form of the temperature dependence of single impurity Kondo scattering. When the temperature is much greater than the Kondo temperature ( $T \gg T_K$ ), a logarithmic temperature dependence is expected, i.e.,  $\rho(T) \propto -\ln(T)$ . When the temperature is much below the Kondo temperature ( $T \ll T_K$ ), the temperature dependence becomes  $\rho(T) \propto -T^2$ .

Numerical renormalization group (NRG) is a powerful way to capture both temperature ranges. In the NRG formalism, resistivity,  $\rho(T)$ , can be expressed as a scalable function,  $f(T/T_K)$  [7–9]. In our resistivity results, the high-temperature regime of  $\rho_a$  and  $\rho_b$  can be thought as a weak logarithmic temperature dependence. In addition, the slight upturn above the  $\sim 14$  K peak of  $\rho_c$  can be thought of as a possible  $\rho(T) \propto -T^2$  dependence. However, this range of change is too small. Also, the slight upturn above the  $\sim 14$  K peak in  $\rho_c$  is the region where there is a sample dependence that was discussed previously. We show an attempt of our resistivity data on top of the  $f_K(T/T_K)$  function when  $T_K = 80$  K in Fig. (7)[8, 9].

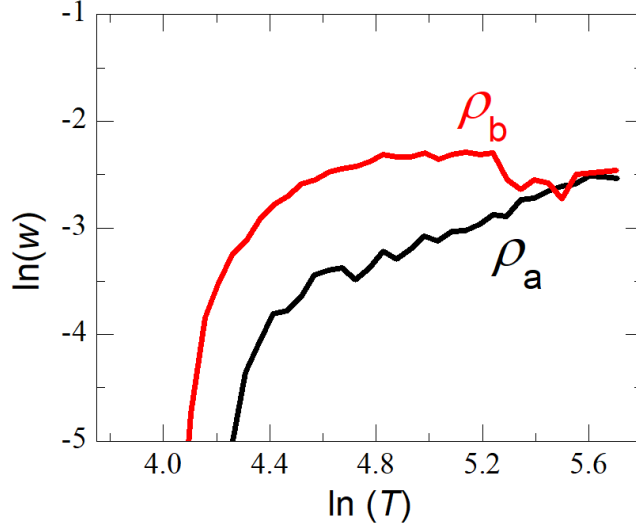


FIG. 8. Zabrodskii plot for investigating hopping conduction transport.

### • Hopping Conduction

As mentioned in the main text, for large resistivities ( $\rho > 0.1\text{m}\Omega$ ,  $d\rho/dT < 0$ , and expected lower dimensionality Fermi surfaces, transport in the localization must be considered. In the localization regime, one expect variable range hopping (VRH)[10]. The functional form of resistivity in the VRH regime is:

$$\rho(T) \propto \exp(T_0/T)^p, \quad (10)$$

where  $p$  is the power that depends on the detail of the theoretical model that ranges from  $1/4$  to  $1/2$ .

An instructive way to visualize the power,  $p$ , of VRH is using the Zabradskii plot[11]. We briefly introduce the method. First, we introduce a functional form,  $w$ :

$$w = -\frac{\partial \ln \rho}{\partial \ln T}. \quad (11)$$

If the resistivity follows a functional form of Eq. (10),

$$w = p \times \left(\frac{T_0}{T}\right)^p. \quad (12)$$

If we plot  $\ln(w)$  vs.  $\ln T$ , a linear slope is  $-p$ . Therefore, for VRH, we would expect a linear plot with a negative slope. In Fig. (8), we plot the Zabradskii plot of  $\rho_a$  and  $\rho_b$  above  $\sim 50$  K. We see that both  $\rho_a$  and  $\rho_b$  do not have a negative slope.

#### IV. MAGNETIZATION ANALYSIS

In the main text, we compared transport data to magnetization. One of the important questions that first need to be answered is whether our transport results can be explained by a standard Kondo lattice or not. To answer this question, an important reference to compare with is magnetization ( $\vec{M}$ ). In a standard Kondo lattice,  $M/H$ , in the linear response regime, we expect the following:

- Above the Kondo temperature ( $T \gg T_K$ ), a Curie-Weiss susceptibility:

$$M/H = \chi_{CW} = \frac{c}{T + \theta}, \quad (13)$$

where  $c$  is a prefactor.

- Below the Kondo temperature ( $T \ll T_K$ ), a constant susceptibility:

$$M/H = \chi \sim \text{constant}. \quad (14)$$

All three directions obey Curie-Weiss behavior at high temperatures. In Fig. (9) (a), we show  $(M/H)^{-1}$  vs. temperature for different magnetic field directions and fixed field magnitudes. The linear behavior above  $\sim 100$  K implies a Curie-Weiss behavior since:

$$(M/H)^{-1} = \chi^{-1} \propto T + \theta. \quad (15)$$

We find  $\theta$  for the a-axis to be -48.68 K. We find  $\theta$  for the b-axis as -111.37 K and c-axis to be -112.93 K. The b- and c- axis may share the same  $\theta$  value, as the fitting values are very close.

Although all three directions fit well with a Curie-Weiss susceptibility, the low temperature behavior neither follows the Curie-Weiss nor a constant susceptibility value. This implies that the magnetization data at low temperatures (below  $\sim 100$ K) requires an understanding beyond a standard Kondo lattice model. Below  $\sim 10$  K, it is well known that  $M/H$  suppresses greatly in the a-axis field direction[12], and even follows a scaling behavior that may be originating from the vicinity of ferromagnetism[1]. We would like to compare our electrical transport results with such non-Kondo behavior contribution of magnetization.

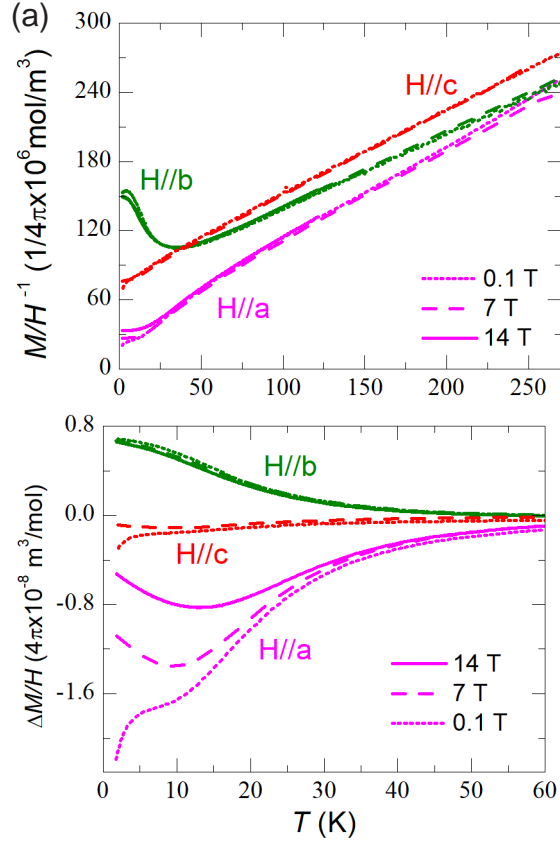


FIG. 9. Magnetization data as a reference. (a)  $(M/H)^{-1}$  vs. temperature. (b)  $\Delta M/H$  vs. temperature.

This non-Kondo, or non-Curie-Weiss susceptibility, contribution of  $M/H$  can be thought as a subleading order temperature dependence. In order to emphasize this contribution, we conveniently subtract the data from the Curie-Weiss susceptibility. We define  $\Delta M/H$  as:

$$\Delta M/H = \chi_{CW} - M/H, \quad (16)$$

where  $\chi_{CW} = c/(T + \theta)$ . Another important note is that  $\Delta M/H > 0$  should be expected in a standard Kondo lattice since  $M/H$  is constant below the Kondo temperature.

We present  $\Delta M/H$  vs temperature for all three directions in Fig. (9) (b). We first comment on the sign of  $\Delta M/H$ . When the magnetic field is directed along the a- and c-axis, we find  $\Delta M/H < 0$ , opposite to a Kondo lattice behavior. When the magnetic field is directed along the b-axis, we find  $\Delta M/H > 0$ . Next we comment on the field dependence.  $\Delta M/H$  for both fields along the a- and c- axis have a field dependence, whereas the data

for field along the b-axis have a very weak field dependence.  $\Delta M/H$  for field along the a- and c-axis, both have peak positions around  $\sim 10$  K, similar to the positions of the peak position of MR when the field is along the a- and c- axis and resistivity along the c-axis. In the following section, we describe the details of MR in all three directions.

## V. MAGNETOTRANSPORT ANALYSIS

In this section, we explain our work of magnetotransport in more detail. In magnetotransport in the normal state of  $UTe_2$ , negative magnetoresistance (MR) is observed in a wide temperature range and field directions. Particularly, we notice that  $\rho_c$  peak near 14 K suppresses greatly by this negative MR when the field direction is along the a-axis.

As a reference, a well-understood source of negative MR in a metallic system is scattering by magnetic impurities.

In the small field limit, the approximate form of resistance as a function of magnetic field would be in the  $T \rightarrow 0$  limit is[13]:

$$R \approx R_0(1 - (\frac{\pi}{2}M)^2) \approx R_0(1 - 0.395\frac{H^2}{T_K^2}) \quad (17)$$

Of course, in our case of  $UTe_2$ , we are not dealing with magnetic impurities in the dilute randomly distributed. We are dealing with a Kondo lattice. In this case, we can think a similar qualitative behavior is expected at temperatures much higher than the coherence temperature. In  $UTe_2$  normal transport, negative MR is also observed at low temperatures when the coherence is expected to develop. In this case, the above negative MR may not be applicable.

An important component to understand magnetic aspects of  $UTe_2$  is the configuration of the uranium atoms within the unit cell. For example, the magnetic easy axis of  $UTe_2$  is along the a-axis due to the uranium chains along that direction. The hard axis is the b-axis where tellurium atoms form a chain and not the uranium atoms. In the c-axis, the uraniums form rungs, so some sort of magnetism is also expected.

As shown in the main text, the peak at  $\rho_c$  suppresses greatly when the magnetic field is along the a-axis direction. We additionally performed a rotation of the sample while the magnetic field is fixed, as shown in Fig. (10). Indeed, as expected from the uranium configurations, the negative MR is greatest along the a-axis and becomes weaker along different

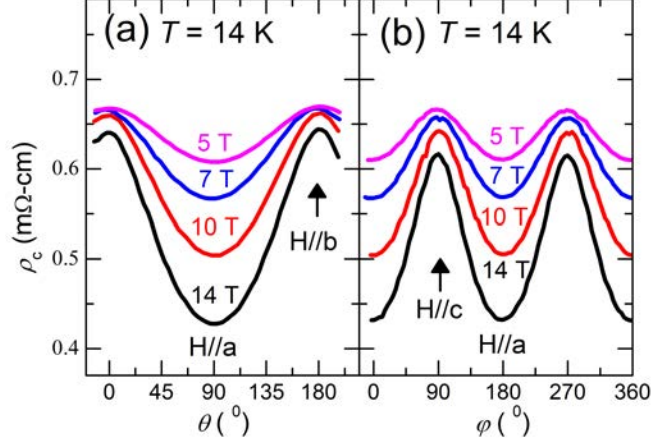


FIG. 10.  $\rho_c$  rotated at a fixed magnetic field (5 T, 7 T, 10 T, and 14 T.) near the peak (14 K). (a) Field rotation is from b- to a-axis. (b) Field rotation is from a- to c-axis.

directions. This rotational magnetotransport study shows that the a-axis dominates. The other directions can be fitted to even powers of cosines from the a-axis direction.  $\rho_c$  when  $H \parallel c$  is also a negative MR compared to zero field, but much weaker negative MR than the a-axis.

Fig. (11) (a) ((b)) shows MR vs. temperature at 14 T for  $\rho_a$  ( $\rho_c$ ). Note that the MR data below 5.4 K for  $\rho_a$ , indicated as dotted lines, was alternatively estimated from a Fermi-liquid-like quadratic temperature dependence fitting parameters:  $\rho = A(H = 14T)T^2 + B(H = 14T)$  since the MR from  $\rho$  vs temperature directly was too noisy.

Comparing Fig. (11) (a) and Fig. (11) (b), except for a systematic MR difference of  $\sim 0.1$ ,  $\rho_a$  and  $\rho_c$  have almost identical MR. This suggests that governing MR behavior does not depend on the direction of the current direction.

Also, notice that the sign, peak positions, and relative magnitudes of MR at different field directions are similar to high field  $\Delta M/H$  (7 T or 14 T data), as shown in Fig. (9). This suggests that MR originates from a non-Kondo contribution of magnetization.

## VI. TRANSPORT AND ARPES COMPARISON

In the main text, we found that the conductivity contribution of the rectangular Fermi surfaces from transport is:

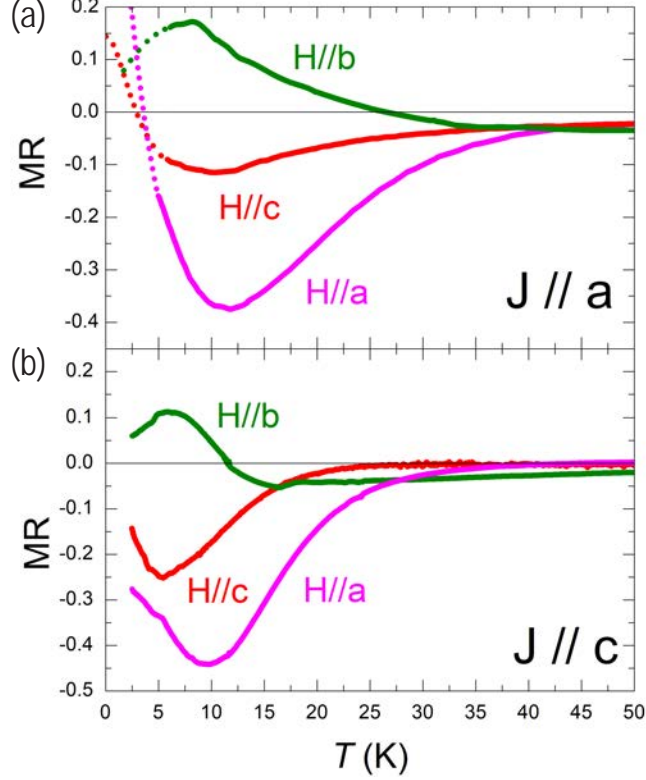


FIG. 11. (Color) MR vs. temperature at 14 T. (a) MR from  $\rho_a$ . Note that the dotted lines are estimated from the Fermi-liquid-like quadratic temperature dependence fitting parameters. (b) MR from  $\rho_c$ .

$$\sigma_{rect} = 1/\rho_a - 1/\rho_c = 1/(0.3m\Omega - cm), \quad (18)$$

We use the size of Fermi surface from ARPES to estimate the carrier density,

$$n_{rect} = \frac{2f}{(2\pi)^2} A_{FS}/a_c \quad (19)$$

, where  $A_{FS}$  is the area under the Fermi surface in the  $ab$  plane,  $a_c$  is the lattice constant in the  $c$ -axis direction, and  $f$  is the formula unit. From Ref.[14], we use the Fermi wave vectors  $k_F^a = 0.408 \times 10^{10}/\text{m}$  and  $k_F^b = 0.245 \times 10^{10}/\text{m}$ . We find  $2n_{rect} = 1.1 \times 10^{22} \text{ 1/cm}^3$ . The Fermi velocity is  $v_F = 3.5 \times 10^5 \text{ m/s}$  and the effective mass is  $m_{rect} = 1.1m_e$ . Using these parameters together with the resistivity data, we find a mobility of  $1.8 \text{ (cm}^2/\text{V-sec)}$ . Alternatively, we can try the inverse feature length as the mean free path ( $5 \times 10^{-10} \text{ m}$ ) from ARPES. The mobility in this case is  $2.3 \text{ (cm}^2/\text{V-sec)}$ . Similarly, the Z-pocket carrier density can be estimated as  $2.4 \times 10^{21} \text{ (1/cm}^3)$ . Using  $\rho_c = 0.6 \text{ m}\Omega\text{-cm}$ , we find a mobility of  $4.3$

( $\text{cm}^2/\text{V-sec}$ ).

Lastly, using  $\rho(T \rightarrow 0)_a = \rho_0 = 15.5\mu\Omega\text{-cm}$  and  $\rho(T \rightarrow 0)_c = \rho_0 = 96.6\mu\Omega\text{-cm}$ , we find the mobility  $\mu = 29.1$  ( $\text{cm}^2/\text{V-sec}$ ) for the quasi-2D pocket and  $26.9$  ( $\text{cm}^2/\text{V-sec}$ ) for the Z-pocket.

## VII. ARPES MEASUREMENTS AND FITTING

ARPES measurements were performed at beamline 4.0.3 at the Advanced Light Source, with a base pressure better than  $5 \times 10^{-11}$  Torr. The sample was cleaved in situ at  $T \sim 20$  K, and the [011] easy-cleave face orientation was confirmed by Laue imaging.

Fig. 3 (b) of the main text presents an analysis of intensity that appears due to quasi-elastic scattering in a momentum region with no band features, as an approximate gauge of the total density of states (DOS). To obtain this, we have subtracted off an estimate of the inelastic Shirley background, as shown in Fig. (12) (a). The Shirley background is approximated as having a derivative that is linearly proportional to the DOS amplitude[15, 16] and is taken to saturate at 90% of the spectral intensity at  $E = 0.45$  eV. The selection of a 90% threshold represents the assumption that overall DOS is very low at  $E = 0.45$  eV, as in DMFT modeling. The uncontrolled nature of this parameter makes the post-subtraction curve unreliable in regions where Shirley background is taken to dominate (particularly  $E > 200$  meV binding energy) but has little impact on the  $E < 100$  meV region near the Fermi level. The rapid change in photoemission amplitude near the Fermi level versus temperature at  $T < 50$  K is visible in the raw data (Fig. (12) (b)) and is not significantly modified by the method selected for background subtraction.

Fig. (13) shows the fitting of the U 6d band in momentum distribution curves (MDC) from Fig. 3(c) of the main text, centered 25 meV from the Fermi level. Integrated intensity of the 6d band along the momentum axis is assumed to remain constant versus temperature, while the momentum-integrated intensity of the background as a function of temperature is assumed to follow the trend presented by the raw data curves in the bottom panel of Fig. (12). These curves are obtained far from band features and are taken to represent an estimate of the overall background intensity, including both elastic and inelastic components. A close lineshape correspondence is difficult to achieve due to the dome-shaped and pillar-like background (see Fig. (14)), however the decline in intensity of the peaks necessitates

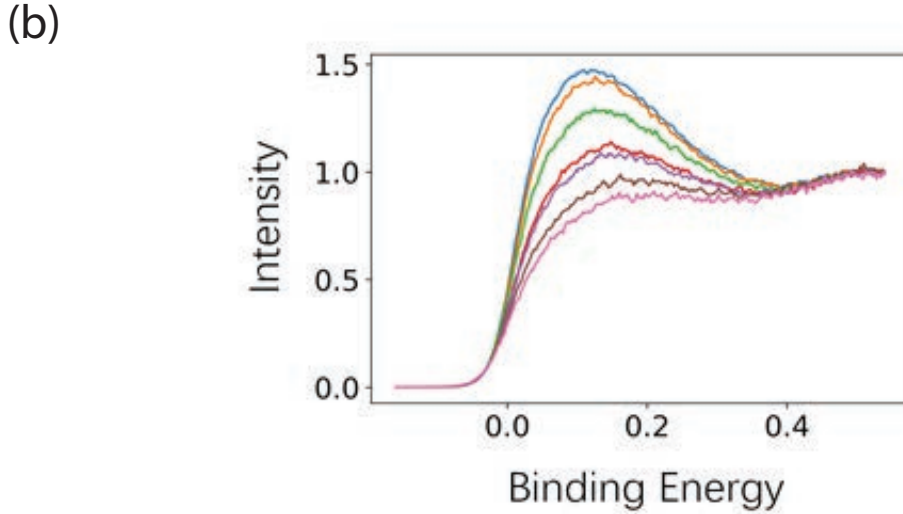
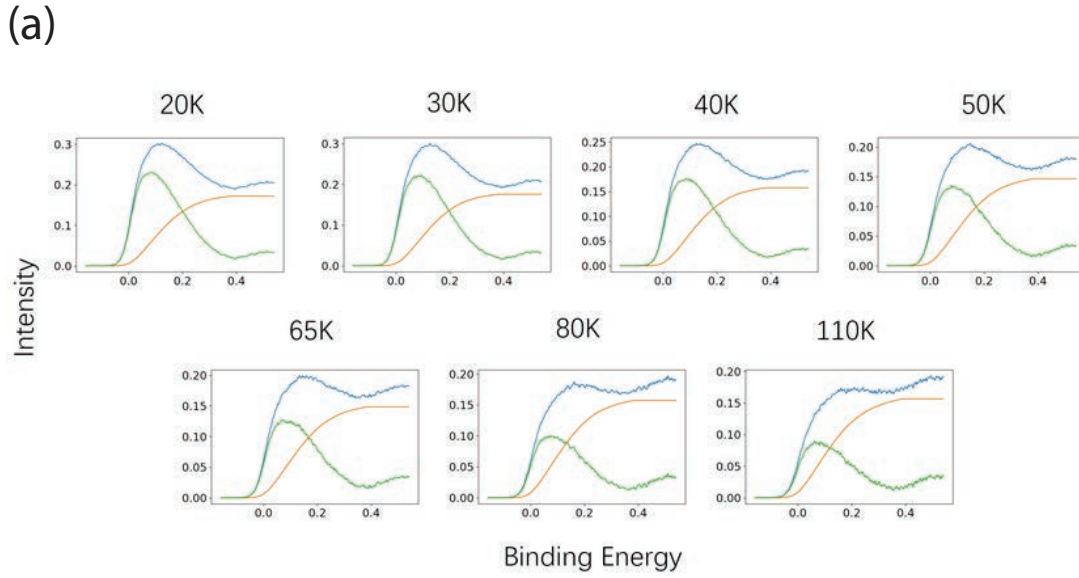


FIG. 12. Shirley subtraction for Fig. 3(b) of the main text. Raw intensity curves are shown in blue, and background subtracted curves are in green. (yellow) A unique Shirley background is obtained by assuming 90% of the spectral intensity at  $E = 0.45$  eV to be background, and taking the difference between raw intensity and the Shirley background to represent density of states. (bottom panel) The temperature dependent trend seen in raw spectral intensity is roughly identical to the background subtracted curves (Fig. 3(b)). Curves in the bottom panel are normalized at  $E = 0.5$  eV binding energy.

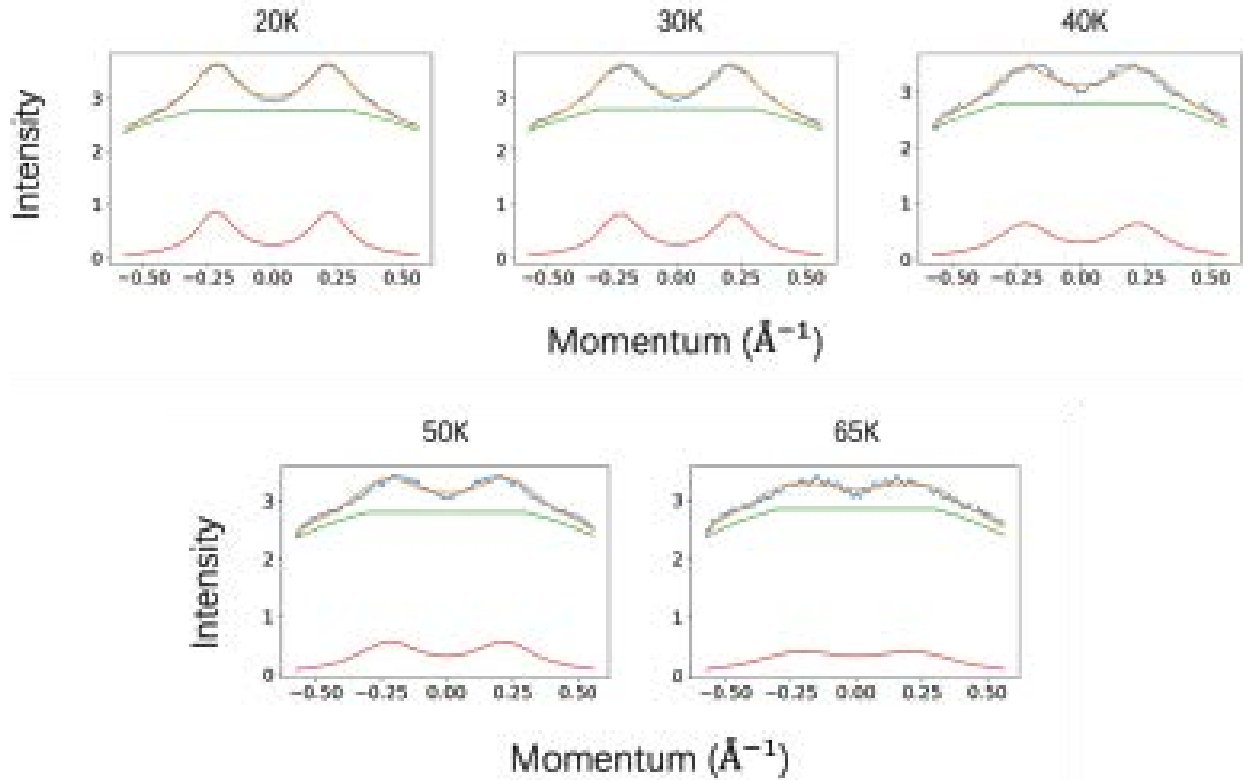


FIG. 13. Peak Width fitting of the curves in Fig. 3(c) of the main text. Data are symmetrized and the band is fitted to a Lorentzian (red curves) on top of a strong background (green curves). Area of the Lorentzian band feature is held constant as a function of temperature, while the background intensity is taken to decline slightly following the trend observed in Fig. (12). The lower right panel shows the deviation observed at  $k > 0.25\text{\AA}^{-1}$  when width is fixed to an artificially small value for the  $T = 65$  K curve

that the 6d band be made broader in momentum at higher temperatures. Uncertainty in the background lineshape is problematic at temperatures greater than  $T > \sim 50$  K, and we have not reported width estimates for temperatures  $T > 65$  K. The primary fitting constraint for  $T = 65$  K is the lineshape at  $k > 0.25\text{\AA}^{-1}$  (see Fig. (12) (b), lower right panel).

---

\* Current address: Department of Physics & Astronomy, Texas Tech University, Lubbock, TX 79409, USA

† paglione@umd.edu

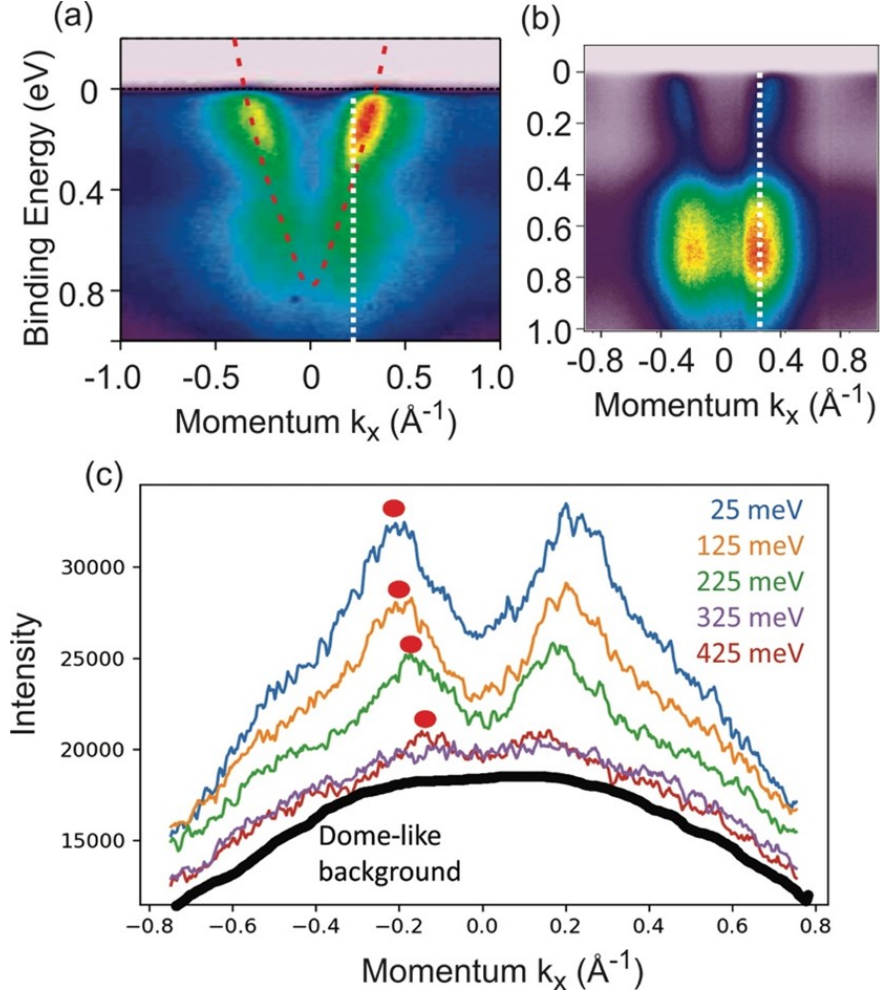


FIG. 14. ARPES background. (a) A column-like background feature is traced in on an ARPES cut intersecting normal emission from the [001] surface. Image reproduced from Ref.[14]. (b) The column-like background feature is traced on an ARPES image of the 6d band dispersion at 7 degrees from normal emission. (c) Constant-energy curves from Fig. 3(a) in the main text are offset on the vertical axis. Spectral intensity of the dispersive features is lower at higher binding energy, revealing a dome-like background (approximated in black).

- [1] S. Ran, C. Eckberg, Q.-P. Ding, Y. Furukawa, T. Metz, S. R. Saha, I.-L. Liu, M. Zic, H. Kim, J. Paglione, *et al.*, *Science* **365**, 684 (2019).
- [2] S. Ran, I.-L. Liu, Y. S. Eo, D. J. Campbell, P. M. Neves, W. T. Fuhrman, S. R. Saha, C. Eckberg, H. Kim, D. Graf, *et al.*, *Nature Physics* **15**, 1250 (2019).
- [3] H. Montgomery, *Journal of applied physics* **42**, 2971 (1971).
- [4] C. Dos Santos, A. De Campos, M. Da Luz, B. White, J. Neumeier, B. De Lima, and C. Shigue,

- Journal of Applied Physics **110**, 083703 (2011).
- [5] Y. S. Eo, K. Sun, C. Kurdak, D.-J. Kim, and Z. Fisk, Phys. Rev. Applied **9**, 044006 (2018).
- [6] I. Miccoli, F. Edler, H. Pfnür, and C. Tegenkamp, Journal of Physics: Condensed Matter **27**, 223201 (2015).
- [7] T. Costi, A. Hewson, and V. Zlatic, Journal of Physics: Condensed Matter **6**, 2519 (1994).
- [8] J. Parks, A. Champagne, T. Costi, W. Shum, A. Pasupathy, E. Neuscamman, S. Flores-Torres, P. Cornaglia, A. Aligia, C. Balseiro, et al., Science **328**, 1370 (2010).
- [9] M. Lee, J. Williams, S. Zhang, C. D. Frisbie, and D. Goldhaber-Gordon, Physical review letters **107**, 256601 (2011).
- [10] Y. Imry, Introduction to mesoscopic physics, 2 (Oxford University Press on Demand, 2002).
- [11] A. Zabrodskii, Philosophical Magazine B **81**, 1131 (2001).
- [12] A. Miyake, Y. Shimizu, Y. J. Sato, D. Li, A. Nakamura, Y. Homma, F. Honda, J. Flouquet, M. Tokunaga, and D. Aoki, Journal of the Physical Society of Japan **88**, 063706 (2019).
- [13] N. Andrei, K. Furuya, and J. Lowenstein, Reviews of modern physics **55**, 331 (1983).
- [14] L. Miao, S. Liu, Y. Xu, E. C. Kotta, C.-J. Kang, S. Ran, J. Paglione, G. Kotliar, N. P. Butch, J. D. Denlinger, et al., Physical Review Letters **124**, 076401 (2020).
- [15] D. A. Shirley, Phys. Rev. B **5**, 4709 (1972).
- [16] S. Hufner, in Photoelectron Spectroscopy (Springer, 1995) pp. 297–366.